J. Fluid Mech. (2018), *vol.* 854, *pp.* 56–87. © Cambridge University Press 2018
doi:10.1017/jfm.2018.622

Convective carbon dioxide dissolution in a closed porous medium at low pressure

Baole Wen[1], Daria Akhbari[2], Li Zhang[3] and Marc A. Hesse[1,2,†]

[1]Institute for Computational Engineering and Sciences, University of Texas at Austin, Austin, TX 78712, USA

[2]Department of Geological Sciences, University of Texas at Austin, Austin, TX 78712, USA

[3]Department of Engineering Mechanics, Tsinghua University, Beijing, 100084, China

(Received 18 August 2017; revised 27 May 2018; accepted 1 August 2018; first published online 31 August 2018)

Motivated by the persistence of natural carbon dioxide (CO_2) fields, we investigate the convective dissolution of CO_2 at low pressure (below 1 MPa) in a closed system, where the pressure in the gas declines as convection proceeds. This introduces a negative feedback that reduces the convective dissolution rate even before the brine becomes saturated. We analyse the case of an ideal gas with a solubility given by Henry's law, in the limits of very low and very high Rayleigh numbers. The equilibrium state in this system is determined by the dimensionless dissolution capacity, Π, which gives the fraction of the gas that can be dissolved into the underlying brine. Analytic approximations of the pure diffusion problem with $\Pi > 0$ show that the diffusive base state is no longer self-similar and that diffusive mass transfer declines rapidly with time. Direct numerical simulations at high Rayleigh numbers show that no constant flux regime exists for $\Pi > 0$; nevertheless, the quantity F/C_s^2 remains constant, where F is the dissolution flux and C_s is the dissolved concentration at the top of the domain. Simple mathematical models are developed to predict the evolution of C_s and F for high-Rayleigh-number convection in a closed system. The negative feedback that limits convection in closed systems may explain the persistence of natural CO_2 accumulations over millennial time scales.

Key words: convection, convection in porous media

1. Introduction

One promising means of reducing the atmospheric emissions of carbon dioxide (CO_2) is to store it in deep geological formations (Metz *et al.* 2005; Orr 2009). When CO_2 is injected into a saline aquifer, it forms an immiscible CO_2-rich vapour phase which is lighter than the aqueous brine and accumulates at the top of the storage formation. The CO_2 dissolves into the underlying brine and forms a diffusive boundary layer beneath the gas–water contact. The brine density increases with aqueous CO_2 concentration and the boundary layer can become unstable and lead to convective overturn within the brine (Weir, White & Kissling 1995; Ennis-King, Preston &

† Email address for correspondence: mhesse@jsg.utexas.edu

https://doi.org/10.1017/jfm.2018.622 Published online by Cambridge University Press

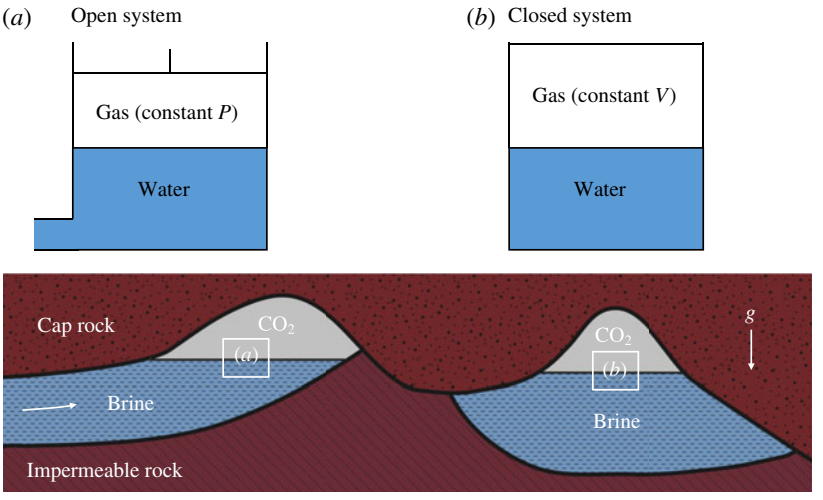


FIGURE 1. (Colour online) Schematic showing natural CO_2 reservoirs with and without structural closure. In system (*a*), the brine can easily move laterally due to the open structure: as CO_2 dissolves in the brine, new brine will be filled into the reservoir, thereby raising the CO_2–brine interface and keeping the gas pressure constant; in system (*b*), no brine can escape from or be filled into the reservoir due to the structural closure, so that the interface is fixed and the dissolution of CO_2 will reduce the gas pressure. We refer to the systems (*a*) and (*b*) as open and closed systems, respectively, and the corresponding idealised rectangular systems are shown at the top.

Paterson 2005). Convective mass transfer can greatly increase the dissolution rate of the injected buoyant CO_2 vapour and hence contributes to safe long-term storage (Neufeld *et al.* 2010; Sathaye *et al.* 2014).

This application has motivated a large amount of recent work on convection in porous media (Huppert & Neufeld 2014; Riaz & Cinar 2014; Emami-Meybodi *et al.* 2015). Work in fluid dynamics has focused on a simplified model problem that considers convection in the brine driven by a constant concentration applied at the top of the domain. At high Rayleigh numbers, the mass transfer is generally characterised by the succession of three dynamic regimes: an initial diffusive decline until the boundary layer becomes unstable, followed by convective dissolution at constant rate, and finally a rapid decline in dissolution rate as the brine saturates and convection shuts down. Most work has focused on determining the onset of convection (Ennis-King *et al.* 2005; Hassanzadeh, Pooladi-Darvish & Keith 2006; Riaz *et al.* 2006; Xu, Chen & Zhang 2006), the convective dissolution rate (Neufeld *et al.* 2010; Pau *et al.* 2010; Hewitt, Neufeld & Lister 2012; Hidalgo *et al.* 2012), and the shut-down of convection (Slim & Ramakrishnan 2010; Hewitt, Neufeld & Lister 2013; Slim *et al.* 2013).

A geological storage site can either be an open or a closed system (see figure 1). Open sites are typically laterally extensive and allow the compensation of pressure changes by brine migration. In an open system, CO_2 dissolution typically leads to a reduction in the volume of the CO_2 vapour over time, while the CO_2 pressure remains approximately constant due to inflow of brine. The aqueous CO_2 concentration beneath the gas–water contact and, therefore, the density difference driving convective dissolution remain constant. In an open system an infinite volume of brine is available,

https://doi.org/10.1017/jfm.2018.622 Published online by Cambridge University Press

so that all injected CO_2 dissolves eventually. Convective dissolution in an open system therefore proceeds at a constant rate until the dense CO_2 saturated fingers begin to interact with the base of the aquifer and dissolution becomes limited by lateral CO_2 transport (Szulczewski, Hesse & Juanes 2013; Unwin, Wells & Woods 2016).

Closed sites are typically fault bounded and do not allow compensation of pressure changes by brine migration. Therefore, the volume of CO_2 vapour in a closed system remains essentially constant over time, and consequently CO_2 dissolution reduces the pressure in the vapour phase (Akhbari & Hesse 2017). This leads to a decline of the aqueous CO_2 concentration beneath the gas–water contact and therefore reduces the density difference driving convective dissolution. In addition, the volume of brine in a closed system is finite and may further limit the dissolution into the brine. Convective dissolution of CO_2 in a closed system is therefore limited by both the pressure drop in the vapour and the saturation of the underlying brine. Previous studies of convection in a closed system have assumed a constant CO_2 concentration at the top boundary, and hence focused on the latter (Slim & Ramakrishnan 2010; Hewitt *et al.* 2013; Slim *et al.* 2013; Slim 2014; Paoli, Zonta & Soldati 2016, 2017). Here we show that the pressure drop in the gas can limit CO_2 dissolution long before saturation of the brine becomes a limiting factor. These negative feedbacks in closed systems are common in experiments on CO_2 dissolution with a pressure range of 0.1–7.0 MPa (Tse & Sandall 1979; Riazi 1996; Wang, Lang & Guo 1996; Zhang, Hyndman & Maini 2000; Sheikha, Pooladi-Darvish & Mehrotra 2005; Farajzadeh, Zitha & Bruining 2007, 2009; Moghaddam *et al.* 2012; Azin *et al.* 2013; Mojtaba *et al.* 2014; Raad, Azin & Osfouri 2015; Ma *et al.* 2017; Shi *et al.* 2018), and in some natural CO_2 reservoirs that serve as analogues for geological CO_2 storage (Akhbari & Hesse 2017).

It is remarkable that many natural CO_2 reservoirs in the continental USA are at pressures significantly less than the critical value 7.39 MPa for a supercritical state, and hence contain CO_2 in a gaseous state (Miocic *et al.* 2016; Akhbari & Hesse 2017). In particular, this is the case for the Bravo Dome natural CO_2 reservoir (with the pressure mostly between 2 MPa and 4 MPa), which is commonly considered as an analogue for engineered CO_2 storage (Broadhead 1987, 1990; Gilfillan *et al.* 2008, 2009; Sathaye *et al.* 2014; Akhbari & Hesse 2017). Therefore, to simplify the analysis and emphasise the essential new feedback, in this study we focus on the low-pressure case (below 1 MPa) and assume that phase behaviour in the closed system is ideal. However, we have used the same modelling approach to describe higher-pressure dissolution experiments for CO_2 in Shi *et al.* (2018) (with the initial pressure ≈ 6 MPa), so that the analysis presented here is not limited to the ideal case, but has practical significance for exploring the dynamics of convective CO_2 dissolution in both laboratory experiments and several underpressured natural CO_2 reservoirs, where CO_2 behaves as a real gas.

Below we give units to avoid confusion that can arise from multiple definitions used for the Henry's law constant. The CO_2 vapour is assumed to be an ideal gas,

$$P_g^* V_g^* = n_g R T, \tag{1.1}$$

where P_g^* (Pa) is the gas pressure, V_g^* (m^3) is the gas volume, n_g (mol) is the amount of gas in moles, R (kg m^2 s^{-2} K^{-1} mol^{-1}) is the universal gas constant, and T (K) is the absolute temperature. The aqueous solution is dilute, so that the local equilibrium between this gas and the dissolved aqueous CO_2 at the gas–water contact is given by Henry's law

$$C_s^* = P_g^* K_h, \tag{1.2}$$

https://doi.org/10.1017/jfm.2018.622 Published online by Cambridge University Press

where C_s^* (mol m^{-3}) is the dissolved gas concentration and K_h (mol m^{-3} Pa^{-1}) is the Henry's law solubility constant. The amount of CO_2 dissolved into a volume of water, V_w^* (m^3), in equilibrium with the gas is therefore given by $n_w = V_w^* K_h P_g^*$ (mol). Since our study is performed in a closed system, the total volume, i.e. $V_g^* + V_w^*$, and the total amount of CO_2, i.e. $n_g + n_w$, remain constant. We note that in modelling of convection, our analysis ignores the slight change in water volume upon CO_2 dissolution as well as the evaporation of water into the gas, both of which are negligible for ideal-gas and certain high-pressure real-gas systems due to the low solubility of CO_2 in water and the low vapour pressure of water at a given temperature of interest in many previous studies (Ma *et al.* 2017; Shi *et al.* 2018). In appendix A, we show that the volume change of the aqueous phase due to the CO_2 dissolution is negligible under ideal conditions and less than 3 % for $P_g^* \leqslant 7$ MPa at $T = 50\,^{\circ}$C.

Consider a closed system that is initially out of equilibrium and contains a gas with a pressure $P_{g,0}^*$ in contact with a finite volume of water containing no dissolved gas. Once the system reaches equilibrium, the normalised final gas pressure and dissolved concentration are given by

$$\frac{P_{g,e}^*}{P_{g,0}^*} = \frac{C_{s,e}^*}{C_{s,0}^*} = \frac{n_{g,e}}{n_{g,e} + n_{w,e}} = \frac{1}{1 + n_{w,e}/n_{g,e}}, \tag{1.3}$$

where the subscript 'e' denotes the final equilibrium state, and $C_{s,0}^* = K_h P_{g,0}^*$ is the dissolved concentration at the interface in local equilibrium with the initial pressure. We define the ratio of dissolved to gaseous CO_2 molecules at global equilibrium as a new dimensionless parameter

$$\Pi = \frac{n_{w,e}}{n_{g,e}} = \frac{V_w^*}{V_g^*} K_h R T. \tag{1.4}$$

This dissolution capacity is a new dimensionless parameter governing both diffusive and convective mass transport in an ideal closed system. The pressure drop in a closed system increases with the dissolution capacity. In the limit of small Π, the pressure drop in the gas becomes negligible and some open system behaviour (i.e. constant C_s^*) is recovered. Thus, most previous investigations (Ennis-King *et al.* 2005; Riaz *et al.* 2006; Pau *et al.* 2010; Hewitt *et al.* 2013; Slim 2014; Paoli *et al.* 2017), which assume a constant CO_2 concentration at the top boundary without new water filled into or moved out of the system, correspond to the particular case $\Pi = 0$ of closed systems.

The remainder of this paper is organised as follows. In the next section, we formulate the dimensional model of convection in the closed porous media system, non-dimensionalise the governing equations, and describe the numerical method to solve these dimensionless equations. In § 3, we give analytic solutions for diffusion in a closed system at early and late times and then investigate the effect of Π on the onset of convection using direct numerical simulations (DNS). In § 4, DNS results are reported for high-Rayleigh-number solutal convection in closed systems, and the corresponding mathematical models of various dissolution quantities are developed for both the quasi-steady convective and the shut-down regimes. In § 5, we use our models to qualitatively estimate the dissolution process in reservoirs with typical parameter values obtained from geological storage sites, and show some moderate-Rayleigh-number DNS results to more comprehensively understand the dynamics of CO_2 dissolution in Bravo Dome natural gas reservoir. Finally, we summarise the key results in § 6.

https://doi.org/10.1017/jfm.2018.622 Published online by Cambridge University Press

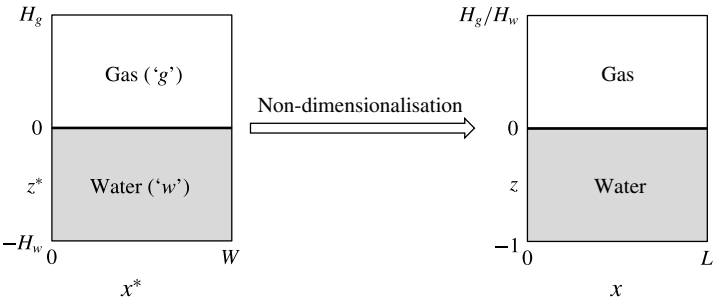


FIGURE 2. Geometry for 2D closed porous media system. The dimensional periodic domain (left) has heights H_g and H_w for the gas and water fields, respectively, and width W. $L = W/H_w$ is the domain aspect ratio for the water field. The continuous dissolution of the gas into the underlying water reduces the gas pressure and then decreases the saturated concentration of water.

2. Problem formulation

2.1. *Dimensional equations*

Consider a two-dimensional (2D), homogeneous, and isotropic porous medium containing gas overlying water (see figure 2). In the limit of negligible capillary forces, the phases are segregated by buoyancy and separated by a sharp interface at $z^* = 0$ (Golding *et al.* 2011; Martinez & Hesse 2016). Therefore, the upper part of the domain, $0 < z^* < H_g$, is occupied only by gas and the lower part, $-H_w < z^* < 0$, is occupied solely by water. Instead of a laterally closed domain we consider a W-periodic domain to simplify the DNS in § 2.3. In terms of the overall mass balance the periodic system is identical to the closed system.

We assume the gas is ideal and well-mixed, so that the pressure is uniform and given by (1.1). The water is incompressible and Boussinesq approximation is valid. We neglect the volume change of water due to the CO_2 dissolution in the modelling of convection (see appendix A), so that the domains containing water and gas are fixed, H_g and H_w are constant, and the interface remains at $z^* = 0$. The system is closed, so that gas and water are coupled through a global mass balance and the local chemical equilibrium along the interface, given by (1.2). Therefore, the governing equations for convection in a closed system comprise a system of partial differential equations (PDEs) describing the convective mass transport in the water and an ordinary differential equation (ODE) for the evolution of the gas. The ODE is coupled to the system of PDEs though the mass flux, F^*, across the interface.

The solute-driven convection in the water is governed by the mass balance of the dissolved gas and the mass and momentum balance of the water itself. The concentration of dissolved gas in the water, C_w^*, evolves due to both diffusive and convective transport following

$$\frac{\partial C_w^*}{\partial t^*} + \boldsymbol{\nabla}^* \cdot (\boldsymbol{u}_w^* C_w^*) = D\nabla^{*2} C_w^*, \tag{2.1a}$$

where D is the diffusivity and $\boldsymbol{u}_w^* = (u^*, w^*)$ the volume-averaged pore velocity. The latter is given by Darcy's law and continuity, so that

$$\boldsymbol{u}_w^* = -\frac{K}{\mu\varphi}(\boldsymbol{\nabla}^* P_w^* + \rho_w^* g \boldsymbol{e}_{z^*}), \tag{2.1b}$$

$$\boldsymbol{\nabla}^* \cdot \boldsymbol{u}_w^* = 0, \tag{2.1c}$$

https://doi.org/10.1017/jfm.2018.622 Published online by Cambridge University Press

where K is the medium permeability, μ is the dynamic viscosity of the fluid, φ is the porosity, P_w^* is the pressure in the water field, g is the acceleration of gravity and $\boldsymbol{e}_{z^*}$ is a unit vector in the z^* direction. The density, ρ_w^*, is assumed to be a linear function of the concentration

$$\rho_w^* = \rho_0^* + \Delta\rho_0^* \frac{C_w^*}{C_{s,0}^*}, \tag{2.2}$$

where ρ_0^* is density of the fresh water and $\Delta\rho_0^*$ is the density difference between the fresh water and the saturated water at the initial pressure. The water contains no dissolved gas so that the initial condition is

$$C_w^*|_{t^*=0} = 0 \quad \text{for } z^* < 0. \tag{2.3}$$

The domain is W-periodic in the x^* direction and impermeable to flow at top and bottom. At the bottom of the domain, the boundary conditions are homogeneous:

$$\left.\frac{\partial C_w^*}{\partial z^*}\right|_{z^*=-H_w} = 0 \quad \text{and} \quad w^*|_{z^*=-H_w} = 0. \tag{2.4a,b}$$

The dissolved concentration at the interface is determined by local equilibrium with the gas, so that the boundary conditions at the top are given by

$$C_w^*|_{z^*=0} = C_s^*(t^*) \quad \text{and} \quad w^*|_{z^*=0} = 0. \tag{2.4c,d}$$

The evolution of the dissolved gas concentration at the interface, C_s^*, is determined by mass balance of the gas, given by

$$\frac{\mathrm{d}n_g}{\mathrm{d}t^*} = -AF^*, \tag{2.5}$$

where A is the area of the interface at $z^* = 0$ (in the 2D system, $A = W$) and F^* is the mole flux from the gas into the water. This flux can be evaluated as

$$F^* = D\left.\frac{\partial \overline{C_w^*}}{\partial z^*}\right|_{z^*=0} = \frac{D}{W}\int_0^W \left.\frac{\partial C_w^*}{\partial z^*}\right|_{z^*=0} \mathrm{d}x^*, \tag{2.6}$$

where the overline denotes the horizontal average as defined above. Combining (1.1), (1.2), (2.5), with (2.6) results in the ODE for the evolution of the dissolved concentration at the interface

$$\frac{\mathrm{d}C_s^*}{\mathrm{d}t^*} = -\frac{K_h RT}{H_g}F^* = -\frac{K_h RTD}{H_g}\left.\frac{\partial \overline{C_w^*}}{\partial z^*}\right|_{z^*=0}, \tag{2.7}$$

with the initial condition

$$C_s^*|_{t^*=0} = C_{s,0}^* = K_h P_{g,0}^*. \tag{2.8}$$

This ODE is coupled to the system (2.1) through the flux (2.6).

https://doi.org/10.1017/jfm.2018.622 Published online by Cambridge University Press

2.2. *Dimensionless equations*

A uniform non-dimensionalisation of the model problem is difficult, since the dominant length scales change with time (Riaz *et al.* 2006; Hewitt *et al.* 2013; Slim *et al.* 2013). Porous media convection is governed by the Rayleigh–Darcy number, $Ra = \mathcal{U}\mathcal{H}/D$, where $\mathcal{U}$ and $\mathcal{H}$ are suitable velocity and length scales, respectively (Horton & Rogers 1945; Lapwood 1948). The Rayleigh–Darcy number is effectively a Péclet number and can be interpreted as the ratio between diffusive, $\mathcal{T}_d = \mathcal{H}^2/D$, and advective, $\mathcal{T}_a = \mathcal{H}/\mathcal{U}$, time scales, $Ra = \mathcal{T}_d/\mathcal{T}_a$.

The natural velocity scale in the convecting system is the buoyancy velocity, $\mathcal{U} = K\Delta\rho_0^* g/(\mu\varphi)$. Convection initiates along the top boundary and penetrates into the domain at a speed proportional to $\mathcal{U}$. At early time, after onset of convection but before convection spans the entire domain, the thickness of the diffusive boundary layer, $D/\mathcal{U}$, provides an natural length scale (Riaz *et al.* 2006). At later time, convection interacts with the bottom boundary and the domain height, H_w, is the appropriate length scale. Advection and diffusion balance across the boundary layer, so that the advective and diffusive time scales are identical at early time, $\mathcal{T}_{ad} = D/\mathcal{U}^2$ (Slim 2014). Scaling the system by the thickness of the diffusive boundary layer sets the Rayleigh number to unity and highlights the universal behaviour of the early convecting system.

Below we assume that $\mathcal{T}_d$ and $\mathcal{T}_a$ are based on H_w, appropriate for the long-term evolution of the convecting system. These two late time scales are related to the early time scale as follows:

$$\mathcal{T}_{ad} = \mathcal{T}_a/Ra_0 = \mathcal{T}_d/Ra_0^2, \quad \text{where } Ra_0 = \frac{K\Delta\rho_0^* g H_w}{\varphi\mu D} \tag{2.9}$$

is the Rayleigh–Darcy number based on the initial density difference. In a convecting system $Ra_0 \gg 1$, so that the magnitudes of these time scales differ significantly.

To allow reduction of the governing equations to a purely diffusive system we choose the diffusive time, $\mathcal{T}_d = H_w^2/D$, as characteristic time scale and define the following dimensionless variables:

$$\boldsymbol{x} = \frac{\boldsymbol{x}^*}{H_w}, \quad \rho = \frac{\rho_w^*}{\Delta\rho_0^*}, \quad t = \frac{t^*}{\mathcal{T}_d}, \quad \boldsymbol{u} = \frac{\boldsymbol{u}_w^*}{\mathcal{U}}, \quad \tilde{P} = \frac{P_w^*}{\Delta\rho_0^* g H_w}, \quad C = \frac{C_w^*}{C_{s,0}^*}. \tag{2.10a–f}$$

Substituting these scales into (2.1) leads to the following dimensionless governing equations:

$$\frac{\partial C}{\partial t} + Ra_0\boldsymbol{u}\cdot\boldsymbol{\nabla}C = \nabla^2 C, \tag{2.11a}$$

$$\boldsymbol{u} = -\boldsymbol{\nabla}P - C\boldsymbol{e}_z, \tag{2.11b}$$

$$\boldsymbol{\nabla}\cdot\boldsymbol{u} = 0, \tag{2.11c}$$

where $P = \tilde{P} + (\rho_0^*/\Delta\rho_0^*)z$ and Ra_0 is the initial Rayleigh–Darcy number defined in (2.9). This system of equations is solved subject to the dimensionless initial condition

$$C|_{t=0} = 0 \quad \text{for } z < 0, \tag{2.12}$$

and boundary conditions

$$\left.\frac{\partial C}{\partial z}\right|_{z=-1} = w|_{z=-1} = 0; \quad C|_{z=0} = C_s(t) \quad \text{and} \quad w|_{z=0} = 0, \tag{2.13a–c}$$

https://doi.org/10.1017/jfm.2018.622 Published online by Cambridge University Press

where C_s is the dimensionless dissolved concentration at the interface. Note that here C_s is also identical to the normalised gas pressure from Henry's law and ideal-gas law, i.e. $C_s = P_g^*/P_{g,0}^*$. The evolution of C_s is given by the following ODE and initial condition:

$$\frac{\mathrm{d}C_s}{\mathrm{d}t} = -\Pi \left.\frac{\partial \overline{C}}{\partial z}\right|_{z=0} \quad \text{and} \quad C_s|_{t=0} = 1, \tag{2.14a,b}$$

where Π is the dissolution capacity, defined by (1.4). The equation (2.14) actually works as a Robin boundary condition for the concentration field in the water. Similar boundary conditions are also utilised in some thermal porous media convection with imperfectly conducting boundaries (Wilkes 1995; Kubitschek & Weidman 2003; Barletta & Storesletten 2012; Barletta, Tyvand & Nygøard 2015; Hitchen & Wells 2016), where the heat flux depends linearly on the surface temperature and a dimensionless parameter *Bi*, the Biot number, is characterised to represent the rate of thermal transport across the boundary. However, unlike those thermal convection studies, here the time-dependent equation (2.14) couples a global mass balance between two subsystems (i.e. the gas and the water) and is always uniform along the gas–water interface.

The dimensionless dissolution flux F that couples (2.11) and (2.14) can be expressed as

$$F(t) = \left.\frac{\partial \overline{C}}{\partial z}\right|_{z=0} = \frac{1}{L}\int_0^L \left.\frac{\partial C}{\partial z}\right|_{z=0} \mathrm{d}x. \tag{2.15}$$

Comparing (2.6) and (2.15), the scale for the flux is $\mathcal{F} = DC_{s,0}^*/H_w$, so that $F = F^*/\mathcal{F}$. To measure the magnitude of the CO_2 dissolution, we define the volume-averaged concentration in the water

$$\overline{\overline{C}}(t) = \frac{\int C \,\mathrm{d}\boldsymbol{x}}{V_w}, \tag{2.16}$$

and mass conservation of the whole system requires that

$$C_s + \Pi \overline{\overline{C}} \equiv 1. \tag{2.17}$$

While the governing equations have been scaled by the diffusion time $\mathcal{T}_d$, other scales may be appropriate for the discussion of early and late phenomena. Therefore, we define the following diffusive, advective (or convective), and advective–diffusive dimensionless times:

$$t = t_d = t^*/\mathcal{T}_d, \quad t_a = t^*/\mathcal{T}_a, \quad \text{and} \quad t_{ad} = t^*/\mathcal{T}_{ad}, \tag{2.18a–c}$$

respectively.

2.3. *Numerical method*

To solve these governing equations numerically, it is convenient to first introduce a stream function ψ to describe the 2D fluid velocity, so that $\boldsymbol{u} = (u, w) =$

https://doi.org/10.1017/jfm.2018.622 Published online by Cambridge University Press

$(\partial_z\psi, -\partial_x\psi)$ and the continuity equation (2.11*c*) is satisfied. Then the dimensionless equations (2.11*b*) and (2.11*a*) can be written as

$$\nabla^2\psi = \partial_x C, \tag{2.19}$$

$$\partial_t C + Ra_0(\partial_z\psi\,\partial_x C - \partial_x\psi\,\partial_z C) = \nabla^2 C, \tag{2.20}$$

where ψ satisfies L-periodic boundary conditions in x and homogeneous Dirichlet boundary conditions in z.

In our study, the equations (2.19) and (2.20) were solved numerically using a Fourier–Chebyshev-tau pseudospectral algorithm (Boyd 2000). For temporal discretisation, a third-order-accurate semi-implicit Runge–Kutta scheme (Nikitin 2006) was utilised for computations of the first three steps, and then a four-step fourth-order-accurate semi-implicit Adams–Bashforth/backward-differentiation scheme (Peyret 2002) was used for computation of the remaining steps. At each step, we updated C_s by solving (2.14*a*) explicitly using a two-step Adams–Bashforth algorithm.

3. Diffusion solution and onset of convection

At sufficiently small Rayleigh number, the system is stable to perturbations and mass transfer is purely diffusive. When the Rayleigh number is above some critical value, the diffusive boundary layer becomes unstable and induces downward moving convective fingers which significantly increase the rate of CO_2 dissolution into the water. In § 3.1 we provide analytic approximations for the diffusive base state in the closed system and then study the onset of the convection using DNS in § 3.2.

3.1. *Diffusion solution*

In a stable system $\boldsymbol{u} = 0$ and mass transport is purely diffusive, so that (2.11) reduces to the one-dimensional diffusion equation

$$\frac{\partial C}{\partial t} = \frac{\partial^2 C}{\partial z^2} \quad \text{on } z \in [-1, 0], \tag{3.1}$$

with (2.12) and (2.13) as initial and boundary conditions, respectively. A complete closed form solution is not available, but solutions in different limiting cases can be obtained by using a Laplace transform. For $\Pi = 0$, the classic series solution for diffusion in a finite domain can be written as

$$C(z, t) = \sum_{n=0}^{\infty}(-1)^n \left[2 - \operatorname{erf}\left(\frac{-z}{2\sqrt{t}} + \frac{n}{\sqrt{t}}\right) - \operatorname{erf}\left(\frac{z}{2\sqrt{t}} + \frac{n+1}{\sqrt{t}}\right)\right], \tag{3.2}$$

on $z \in [-1, 0]$ (Crank 1975). This solution reduces to simple error function solution for diffusion in a semi-infinite domain at early time, $t \ll 1$. For $\Pi > 0$, a closed form solution can only be found at early time when the domain is effectively semi-infinite. This solution is then given by

$$C(z, t) = \mathrm{e}^{\Pi^2 t - \Pi z}\left[1 + \operatorname{erf}\left(-\Pi\sqrt{t} + \frac{z}{2\sqrt{t}}\right)\right] \quad \text{on } z \in (-\infty, 0], \tag{3.3}$$

and reduces to the standard error function solution in the limit $\Pi = 0$ (Sheikha *et al.* 2005; Kim, Yoon & Choi 2006). Hereafter, (3.3) is referred to as the early-time solution. We note that these solutions are not self-similar in $z/\sqrt{t}$, if $\Pi > 0$.

https://doi.org/10.1017/jfm.2018.622 Published online by Cambridge University Press

At late time, the diffusive front interacts with the bottom boundary and the finiteness of the domain affects the solution. For $\Pi > 0$, the full solution in the Laplace transform variable is given by

$$\hat{C}(z, s) = \frac{\cosh(\sqrt{s}(z+1))}{s\cosh(\sqrt{s}) + \Pi\sqrt{s}\sinh(\sqrt{s})} \quad \text{on } z \in [-1, 0], \tag{3.4}$$

but the inverse Laplace transform of this expression does not lead to a closed form expression. Instead, a series solutions can be obtained via Cauchy's residue theorem (Duffy 2004). This requires the poles, s_k, of (3.4), which are given implicitly by the roots of

$$\tan(p) = -\frac{p}{\Pi}, \tag{3.5}$$

where $s = -p^2$ (Zhang, Hesse & Wang 2017). From the definition of the inverse Laplace transform and Jordan's lemma (Schiff 1999), the solution is then given by

$$C(z, t) = \mathcal{L}^{-1}\{\hat{C}(z, s)\} = \frac{1}{2\pi\mathrm{i}} \lim_{\widetilde{T}\to\infty} \int_{r-\mathrm{i}\widetilde{T}}^{r+\mathrm{i}\widetilde{T}} \hat{C}(z, s)\mathrm{e}^{st}\,\mathrm{d}s = \sum_{n=0}^{\infty} a_n \mathrm{e}^{-p_n^2 t}, \tag{3.6}$$

where the coefficients of the residues for the simple poles are

$$a_n = \lim_{s\to s_n}(s - s_n)\hat{C}(z, s) = \begin{cases} \dfrac{1}{1+\Pi} & n = 0, \\ \dfrac{2\Pi\cos(p_n z) + 2p_n\sin(p_n z)}{\Pi^2 + \Pi + p_n^2} & n \geqslant 1. \end{cases} \tag{3.7}$$

At late times (3.6) is dominated by lowest-order terms and the equilibrium solution is given by the zeroth-order term

$$\lim_{t\to\infty} C = \frac{1}{1+\Pi}. \tag{3.8}$$

The equilibrium solution is constant and entirely determined by the dissolution capacity, Π. At equilibrium, $C = C_s = \overline{\overline{C}}$, so that (3.8) is consistent with the equilibrium condition from overall mass balance (1.3) and mass conservation (2.17). The equilibrium concentration declines rapidly with increasing dissolution capacity, as a decreasing amount of gas dissolves into an increasing amount of water.

The low-order terms in (3.6) generally capture the late-time behaviour, but a large number of modes is needed to describe the solution at early time. We therefore truncate the sum in (3.6) to obtain a late-time approximation and combine it with the early-time solution, given by (3.3), to describe the full evolution. Figure 3(*a*) shows this composite solution for the concentration on the interface, $C_s(t) = C|_{z=0}$, and a numerical solution using the algorithms described in § 2.3 matches this composite analytic solution well. For this comparison, the numerical solution was initialised with (3.3) evaluated at $t = 4 \times 10^{-5}$ to avoid oscillations arising from the discontinuity between the initial and the boundary conditions.

The early-time solution gives insight into the effect that Π has on the diffusive mass transport in a closed system. The concentration on the interface and the flux across the interface are given by

$$C_s(t) = C(t, 0) = \mathrm{e}^{\Pi^2 t}[1 + \mathrm{erf}(-\Pi\sqrt{t})], \tag{3.9a}$$

$$F(t, 0) = -\Pi\mathrm{e}^{\Pi^2 t}[1 + \mathrm{erf}(-\Pi\sqrt{t})] + \frac{1}{\sqrt{\pi t}}, \tag{3.9b}$$

https://doi.org/10.1017/jfm.2018.622 Published online by Cambridge University Press

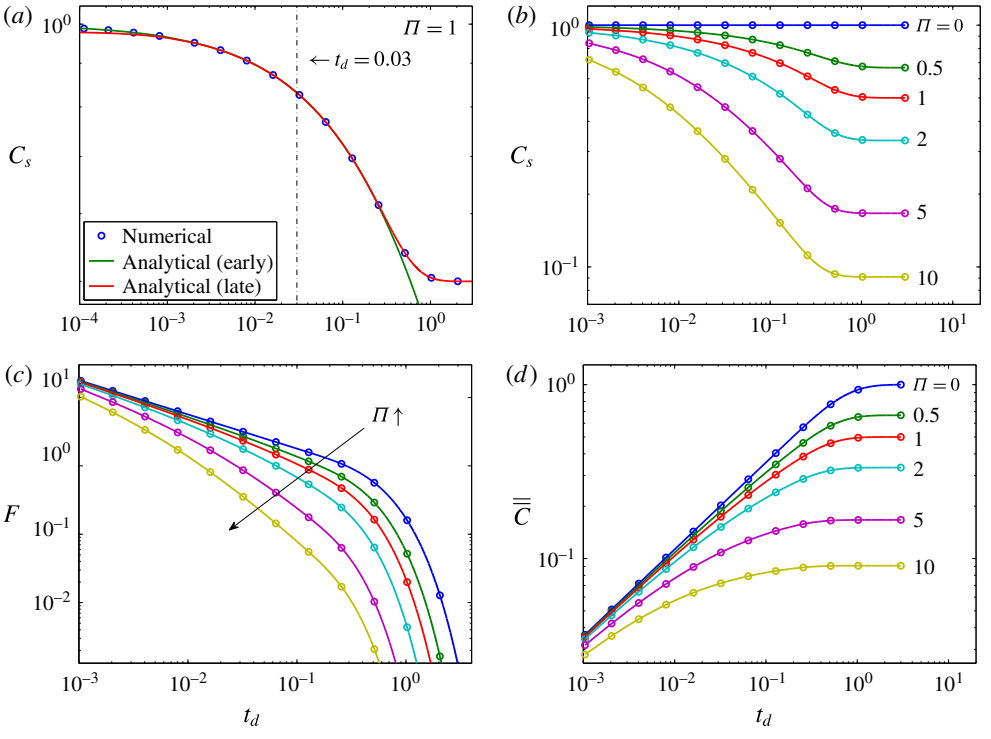


FIGURE 3. (Colour online) Comparisons between numerical and analytic diffusion solutions in the closed system. Circles, numerical solution (the spacing of symbols does not reflect the time steps used in computations); solid lines, analytic solution. In (*a*), the solutions (3.3) and (3.6) are valid, respectively, at early and late times; in (*b–d*) and for $\Pi > 0$, the early-time solution is used as the composite analytic solution at $t_d \leqslant 0.03$ and the late-time solution is used at $t_d > 0.03$. Ten modes (i.e. $0 \leqslant n \leqslant 9$) are utilised to calculate the analytic solutions (3.2) and (3.6). However, our study indicates that for $t_d \geqslant 0.1$, two modes (i.e. $n = 0,\ 1$) of the late-time solution (3.6) are enough to retain a 99 % accuracy of the quantities showing in (*b–d*).

for $t \ll 1$. In the limit of $\Pi = 0$, C_s becomes constant, while for $\Pi > 0$, C_s declines ever more rapidly with increasing Π, as shown in figure 3(*b*). For $\Pi > 0$, the period for which $C_s > 0.99$, i.e. approximately constant, is $t < 0.009/\Pi$, so that the decline in C_s begins earlier with increasing Π. At $\Pi = 0$, F declines as $t^{-1/2}$ at $t \ll 1$, but figure 3(*c*) shows that the flux in the closed system with $\Pi > 0$ does not follow a simple power law, since the rapid decline of C_s at early time reduces the diffusive flux much faster.

The negative feedback introduced by the mass balance constraint in a closed system significantly slows down both the rate of dissolution and the total amount that can be dissolved. However, the time required to reach global equilibrium, $t \approx 1$, remains approximately constant for different Π, as the reduction in flux is offset by the reduction in the equilibrium concentration (see figure 3*d*).

3.2. *Onset of convection*

The diffusive boundary layer will grow with time as the CO_2 continuously dissolves into the water. When the diffusion layer becomes thick enough, the CO_2-rich water,

https://doi.org/10.1017/jfm.2018.622 Published online by Cambridge University Press

which is heavier than the underlying fresh water, can become unstable under the influence of gravity and sink in plumes of heavy CO_2-rich fluid. This phenomenon, known as onset of convection, has been studied extensively by using linear stability analysis and DNS (Ennis-King *et al.* 2005; Hassanzadeh *et al.* 2006; Riaz *et al.* 2006; Xu *et al.* 2006; Kim *et al.* 2008; Javaheri, Abedi & Hassanzadeh 2010; Pau *et al.* 2010; Slim & Ramakrishnan 2010; Elenius & Johannsen 2012; Kim & Choi 2012; Elenius, Nordbotten & Kalisch 2014; Slim 2014; Tilton & Riaz 2014; Kim 2015). A full hydrodynamic stability analysis for the closed system is beyond the scope of this contribution, but we provide DNS that illustrate the effect of Π on the onset of convection. Simulations are conducted for a discrete set of Ra_0 and Π in a 2D domain with aspect ratio $L = 10^5/Ra_0$.

The concentration field $C(\boldsymbol{x}, t)$ can be decomposed into a transient diffusive base state $C_d(z, t)$ plus a fluctuation $\widetilde{C}(\boldsymbol{x}, t)$, namely,

$$C(\boldsymbol{x}, t) = C_d(z, t) + \widetilde{C}(\boldsymbol{x}, t), \tag{3.10}$$

where the diffusion solution C_d is a composite analytic solution as in figure 3 and the fluctuation term can be expressed as

$$\widetilde{C}(\boldsymbol{x}, t) = \sum_{n=-N/2}^{N/2} \hat{C}_n(z, t) \mathrm{e}^{\mathrm{i}nkx}, \tag{3.11}$$

where $k = 2\pi/L$ is the fundamental wavenumber and N is the horizontal truncation mode number. In our DNS, the initial condition is the early-time solution at $t = 1/Ra_0^2$, corresponding to $t_{ad} = 1$, with random perturbations within the top diffusion layer. For the purpose of this study we define the onset of convection as the earliest time when the norm of the amplitude $\hat{C}_n$ starts to grow.

For $\Pi = 0$, the system of equations (2.11) becomes parameterless in the advective–diffusive scheme by rescaling $\boldsymbol{x} = \boldsymbol{x}_{ad}/Ra_0$ and $t = t_{ad}/Ra_0^2$, so that Ra_0 becomes the height of the rescaled layer and the solution is universal before the fingertips reach the bottom boundary. As shown in figure 4, our DNS results indicate that the diffusion solution becomes unstable at $t_{ad} \approx 130$ for $\Pi = 0$. This is consistent with previous work on linear stability analysis, which gives $t_{ad} \approx 146$ (Riaz *et al.* 2006; Javaheri *et al.* 2010; Elenius *et al.* 2014). Nevertheless, for $\Pi > 0$, the system is Ra_0-dependent even in the advective–diffusive scaling, as Ra_0 appears in (2.14) (for advective–diffusive scalings, the time $\mathcal{T}_{ad} = \mathcal{T}_d/Ra_0^2$ and the length $\mathcal{H}_{ad} = H_w/Ra_0$). The onset time in a closed system therefore depends on both Ra_0 and Π (see figure 4). For small Ra_0 the diffusive boundary layer has to grow to a larger thickness before instability occurs. This allows the negative feedback in a closed system to reduce the diffusive flux and to increase the onset time with increasing Π (see figures 3*c* and 4). At sufficiently large Ra_0, however, the onset occurs before the negative feedback in a closed system has reduced the diffusive flux, so that the onset time is independent of Π.

4. Numerical simulations and mathematical models at large Ra_0

To study the dynamics and mass transport of solutal convection in the closed porous media system, DNS were performed at $Ra_0 = 20\,000$ for $\Pi = 0$, 0.5, 1, 2, 5 and 10 in a 2D domain with the aspect ratio $L = 10^5/Ra_0$. In these computations, 8192

https://doi.org/10.1017/jfm.2018.622 Published online by Cambridge University Press

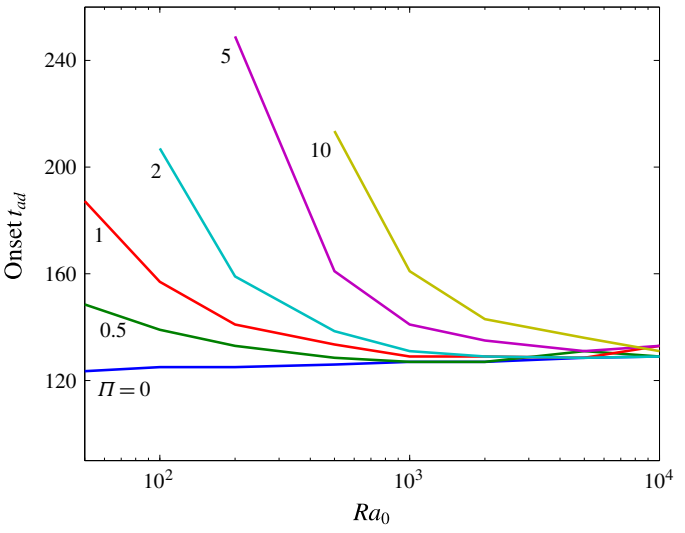


FIGURE 4. (Colour online) Variation of onset time as a function of Rayleigh number and dissolution capacity. For $\Pi \geqslant 2$, The diffusion solution becomes stable at sufficiently small Ra_0 where instability has set in for $\Pi = 0$. In closed systems, the onset of convection is not affected by Π at large Ra_0, but delayed at small Ra_0 with increasing Π due to the reduction of dissolution flux from the negative feedback of the pressure drop in gas.

Fourier modes were utilised in the lateral discretisation, 385 Chebyshev modes were used in the vertical discretisation, and the time step is $\Delta t = 10^{-8}$. Moreover, the early-time solution for the diffusive base state, given by (3.3), at time $t = 25/Ra_0^2$ (or $t_{ad} = 25$) was used as the initial condition for the concentration field, and a small random perturbation was added as a noise within the upper diffusive boundary layer to induce the convective instability. Although the results only from $Ra_0 = 20\,000$ were utilised for following analysis, it will be shown at the end of § 4.2 that our mathematical models are also applicable to other large Rayleigh numbers.

4.1. *DNS results*

Convection at $\Pi = 0$ exhibits a succession of different flow regimes defined by the behaviour of the solute flux (Riaz *et al.* 2006; Slim 2014; Tilton & Riaz 2014). In this study, we distinguish the following regimes defined in figure 5(*a*): an initial 'diffusion-dominant' regime, followed by the 'flux-growth and plume-merging' and 'quasi-steady' convective regimes, and the final 'shut-down' of convection. Below we consider the effect of dissolution capacity, Π, on these regimes in turn and show that the effect increases with time.

The 'diffusion-dominant' regime is not significantly affected by Π, due to the early onset of convection at high Ra_0. This prevents the reduction of C_s at the interface (see figure 5*b*), so that the flux exhibits a diffusive decay, $F \sim (\pi t)^{-1/2}$. This behaviour continues up to $t_a \approx 3000/Ra_0$ (i.e. $t_{ad} \approx 3000$) even after perturbations have begun to grow linearly, since the nascent fingers are still encompassed within the relatively thick diffusive boundary layer.

During the 'flux-growth and plume-merging' regime the boundary layer scallops and the penetration of unsaturated fluid to the interface increases the flux to a maximum.

https://doi.org/10.1017/jfm.2018.622 Published online by Cambridge University Press

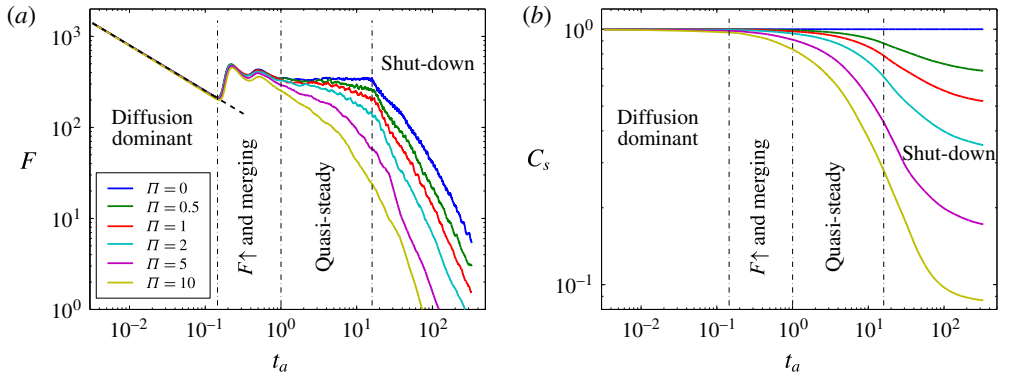


FIGURE 5. (Colour online) Evolution of the dissolution flux F and the interface concentration C_s in time at $Ra_0 = 20\,000$ for different Π. Solid lines, DNS results; dashed lines in (*a*), purely diffusive flux $F \sim (\pi t)^{-1/2}$ for $\Pi = 0$. In both (*a*) and (*b*), the four dynamical regimes are delineated using dot-dashed lines based on the flow characteristics at $\Pi = 0$. Generally, these four regimes still exist for $\Pi > 0$; however, for various Π the time of transitions may be different, e.g. as analysed below the onset of the shut-down regime will be delayed at a higher Π. At sufficiently large Ra_0, Π starts to affect the convection in the flux-growth and plume-merging regime; and in the quasi-steady convective regime, the flux for $\Pi > 0$ does not remain constant due to the decay of the interface concentration C_s.

The evolution of the finger-root concentration in figure 6(*a*) shows that fingers start to travel laterally, which leads to merging of neighbours and a coarsening of the pattern. Due to the short time scales, the basic flow characteristics, e.g. the horizontal-mean finger width δ and magnitude of horizontal-mean downward velocity, w_d, are still not affected by Π (see figure 6*b*,*c*). However, the decrease of the interface concentration C_s at large Π becomes more evident and begins to reduce the solute flux (see figure 5).

After the convective pattern has coarsened, the flow transitions to a 'quasi-steady' convective regime. At these longer time scales ($t_a \approx 1$), C_s begins to drop rapidly (see figure 5*b*) and the difference between convection for $\Pi = 0$ and $\Pi > 0$ is most pronounced. The dissolution flux for $\Pi = 0$ is constant, while the flux for $\Pi > 0$ decays ever more rapidly with increasing Π (see figure 5*a*). Therefore, despite the name of the convective regime, convection for $\Pi > 0$ is never actually quasi-steady. Independent of Π, small protoplumes are continuously generated at the top boundary, swept sideways, and assimilated into the large fingers that penetrate to greater depth. This generates a typical fish-bone pattern in the evolution of the finger-root concentration (Hewitt *et al.* 2012, also see figure 6*a*) and a columnar large-scale flow pattern in the interior (see figure 7). For $\Pi > 0$, the drop in C_s with time reduces the finger-root concentration and the generation of protoplumes from the upper wall. This leads to a characteristic 'fading fish-bone pattern' for convection in closed systems. As the driving force for convection declines, the wavelength of the large-scale flow pattern coarsens and the downwelling plumes slow down (see figure 6*b*,*c*).

After the fingers reach the lower boundary, the CO_2-rich fluid starts to move upwards with the returning flow. Once this dense fluid reaches the upper boundary, the driving force for convection is decreased, the flux declines rapidly, and eventually the convection is shut down (see figure 8). Previous work on convective shut-down,

https://doi.org/10.1017/jfm.2018.622 Published online by Cambridge University Press

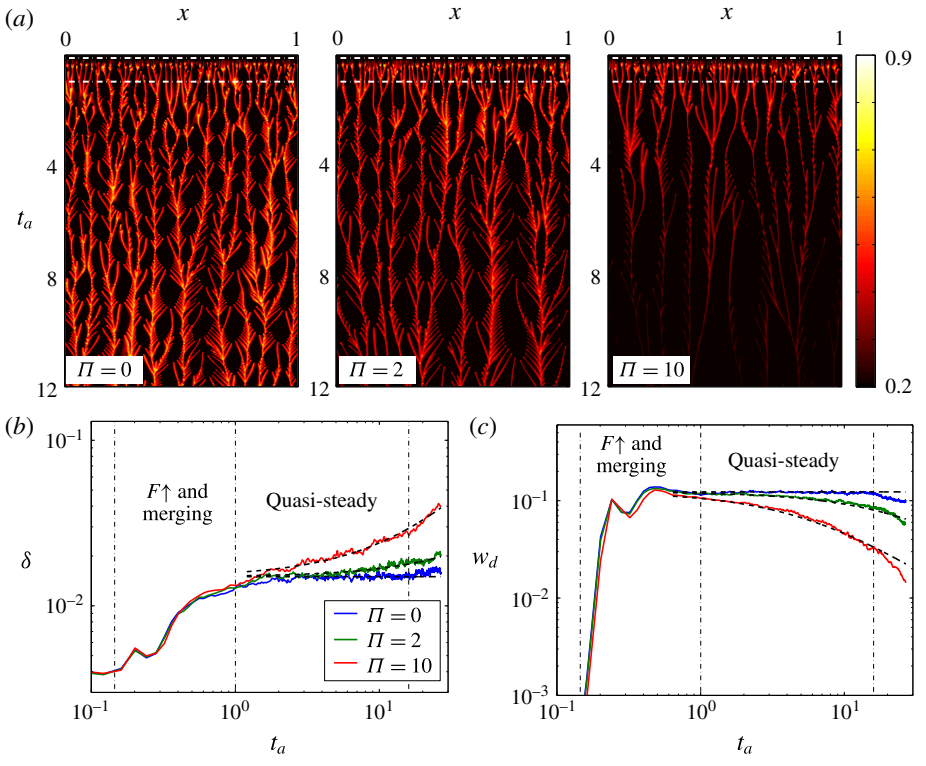


FIGURE 6. (Colour online) Numerical results on $z = -0.01$ at $Ra_0 = 20\,000$ for different Π: evolution in time of (*a*) the concentration profile C, (*b*) the horizontal-mean finger width δ, and (*c*) the magnitude of horizontal-mean downward velocity w_d. In (*a*), only a small portion of x is shown and the two (white) dot-dashed lines indicate the times of transition to the flux-growth and plume-merging regime and the quasi-steady convective regime, respectively, for $\Pi = 0$. In (*b*), the finger width is measured using $\delta = \pi/[\overline{(\partial C'/\partial x)^2}/\overline{C'^2}]^{1/2}$, where $C' = (C - \overline{C})$ is the fluctuation of the concentration field (see more details in Slim 2014). In (*b*) and (*c*), the dynamical regimes are delineated as in figure 5, and we can fit the functional of the mathematical model developed later in (4.5) for C_s in the quasi-steady convective regime to the DNS data of δ and w_d, i.e. $\delta = 0.015(0.006\Pi t_a + 1)$ (dashed) and $w_d = 1/[8.1(0.0168\Pi t_a + 1)]$ (dashed). Before transition to the quasi-steady convective regime, the dynamics are generally not affected by Π. However, in the quasi-steady convective regime, the increase of Π enhances the reduction of the concentration field near the upper wall, resulting in a less vigorous convection in the boundary layer: the plumes become wider, the descending velocity is decreased, and fewer ribs (which represent the protoplumes) exist in the 'fish-bone' pattern and merge with the primary finger roots.

for $\Pi = 0$, shows that the horizontal-mean concentration is well-mixed and almost constant with depth, outside the diffusive boundary layer at the top (Hewitt *et al.* 2013, Slim *et al.* 2013, Slim 2014, also see figure 8*a*), namely,

$$\overline{C} \approx \overline{\overline{C}}(t). \tag{4.1}$$

Based on this observation, theoretical box models were developed to predict the variation of the dissolution flux in time. In this study, our simulation results indicate

https://doi.org/10.1017/jfm.2018.622 Published online by Cambridge University Press

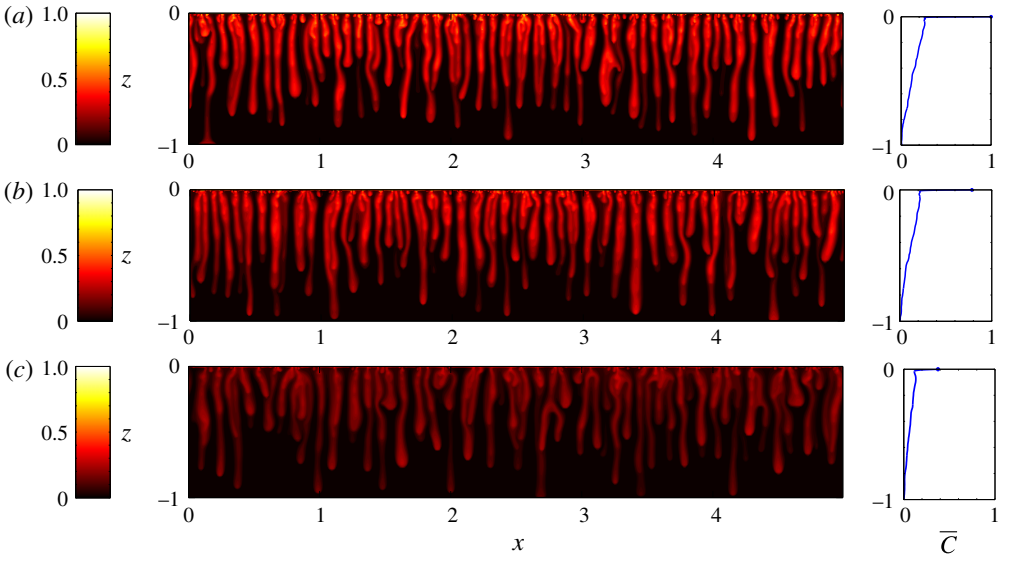


FIGURE 7. (Colour online) Snapshots of the concentration field C and the corresponding horizontal-mean concentration profile $\overline{C}$ from DNS at $Ra_0 = 20\,000$ when the downwelling fingers first reach the bottom wall: (*a*) $\Pi = 0$, $t_a = 7.2$; (*b*) $\Pi = 2$, $t_a = 8$; (*c*) $\Pi = 10$, $t_a = 10$. The dot at the top of $\overline{C}$ denotes the concentration at the upper boundary. The increase of Π reduces the plume-root concentration and decreases the plume descending speed.

that (4.1) is still valid for $0 < \Pi \leqslant 5$. As shown in figure 8, however, for $\Pi \geqslant 10$ the mean concentration profile exhibits a three-layer structure due to the rapid decrease of C_s: near the upper wall is the thin diffusive boundary layer; in the core $\overline{C}$ is nearly independent of z; and near the bottom wall the fluid is stably stratified. In the following section, we will extend these theoretical box models to generic closed systems ($0 < \Pi < 10$) that do not form such a stable stratification at the base.

4.2. *Simple mathematical models*

Here we aim to develop a zero-dimensional representations for the convecting system that capture the evolution of the averaged system quantities, e.g. $C_s(t)$, $F(t)$ and $\overline{\overline{C}}(t)$, in different regimes. This is possible for $\Pi = 0$, since the quasi-steady flux in high-Ra_0 convection can be expressed as a power law of the form

$$F = \alpha\, {Ra_0}^{\beta} \quad \text{for } Ra_0 > Ra^*, \tag{4.2}$$

where $Ra^* \approx 2000$ gives the onset of the power-law scaling for the one-sided penetrative convection considered here (Slim 2014). Our simulations give the following coefficients, $\alpha = 0.0168$ and $\beta = 1$. Similar values for α and β have been found in previous investigations of convection in porous media (Doering & Constantin 1998; Otero *et al.* 2004; Pau *et al.* 2010; Elenius & Johannsen 2012; Hewitt *et al.* 2012; Hidalgo *et al.* 2012; Wen *et al.* 2012, 2013; Hassanzadeh, Chini & Doering 2014; Slim 2014; Wen, Corson & Chini 2015; Wen & Chini 2018), although some authors have argued for $\beta < 1$ (Neufeld *et al.* 2010; Backhaus, Turitsyn & Ecke 2011).

https://doi.org/10.1017/jfm.2018.622 Published online by Cambridge University Press

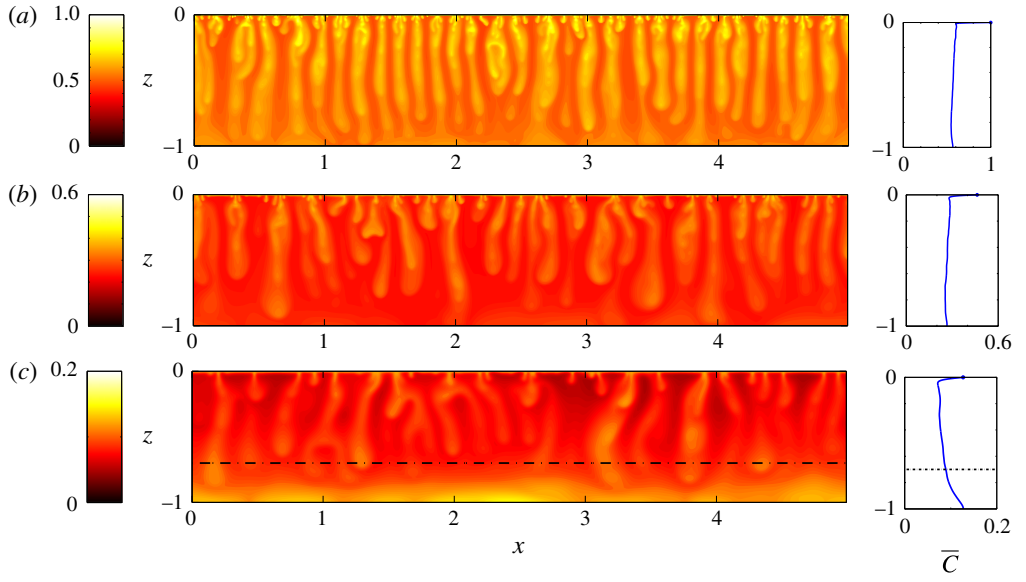


FIGURE 8. (Colour online) Snapshots of the concentration field C and the corresponding horizontal-mean concentration profile $\overline{C}$ from DNS at $Ra_0 = 20\,000$ and $t_a = 50$: (*a*) $\Pi = 0$; (*b*) $\Pi = 2$; (*c*) $\Pi = 10$. The dot at the top of $\overline{C}$ denotes the concentration at the upper boundary. When convection is shut down, the horizontal-mean concentration profile outside the top diffusive boundary layer becomes nearly independent of z. However, at large Π, e.g. $\Pi = 10$ shown in (*c*), due to the rapid decline of C_s at the interface, this system exhibits a three-layer dynamics: above the dot-dashed line is the regular, two-layer shut-down convection as in (*a*,*b*); beneath the dot-dashed line, the fluid is stably stratified and the flow is mainly by diffusion.

Section 4.1, however, shows that no such power-law scaling exists for $\Pi > 0$, as the flux in the quasi-static regime is not constant (see figure 5*a*). Nevertheless, from (2.11*a*) the downward flux beneath the upper diffusive boundary layer at high Ra_0 is largely advective and given by

$$F \approx -Ra_0\,\overline{wC} \approx Ra_0 w_d \overline{C} \sim Ra_0\,\overline{C}^2, \tag{4.3}$$

since the magnitude of the horizontal-mean downward velocity $w_d \sim C$, as shown by (2.11*b*). At $\Pi = 0$, the interface concentration, C_s, is constant and during the quasi-steady regime, $\overline{wC} = -\alpha$ from (4.2) and (4.3). Although F and C_s vary with time in a closed system, equation (4.3) suggests that $F/C_s^2 \sim Ra_0$ in the quasi-static regime. Figure 9(*a*) shows that indeed

$$\frac{F}{C_s^2} = F|_{\Pi=0} = \alpha\, Ra_0, \tag{4.4}$$

for different Π, which allows the extension of previous box models to generic closed systems. Combining (2.14), (2.15) and (4.4) yields the mathematical models for F and C_s in the quasi-steady convective regime:

$$C_s(t_a) = \frac{1}{\alpha \Pi t_a + 1} \quad \text{and} \quad F(t_a) = \frac{\alpha Ra_0}{(\alpha \Pi t_a + 1)^2}. \tag{4.5a,b}$$

https://doi.org/10.1017/jfm.2018.622 Published online by Cambridge University Press

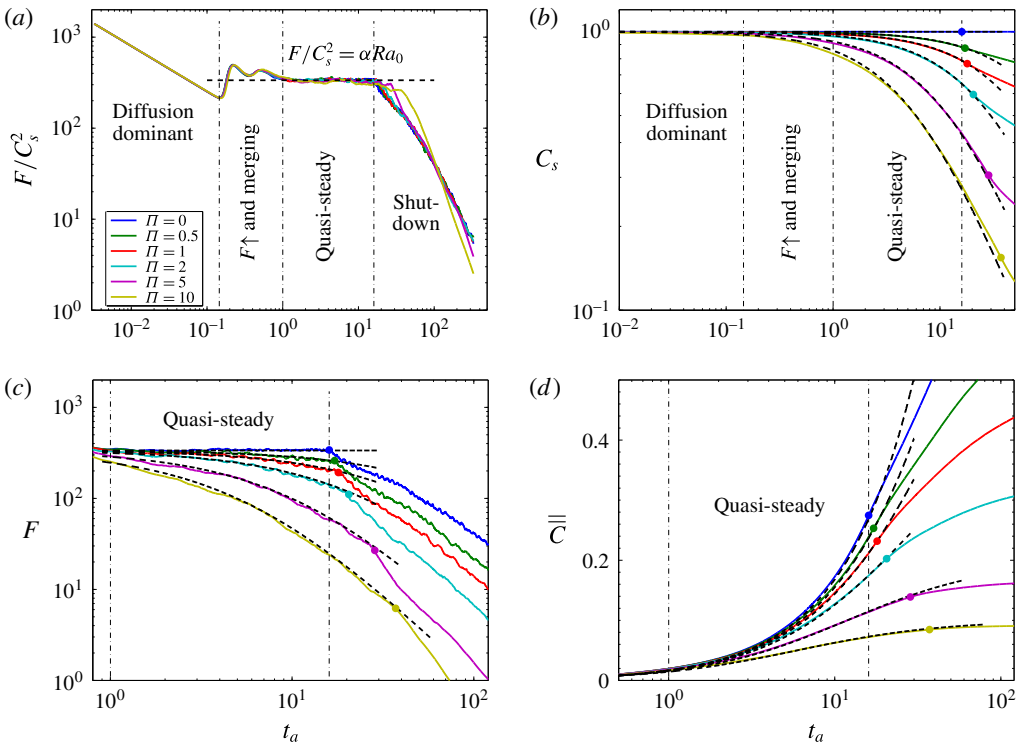


FIGURE 9. (Colour online) Mathematical models for the quasi-steady convective regime in closed systems at $Ra_0 = 20\,000$: (*a*) evolution of the rescaled dissolution flux F/C_s^2 in time; (*b–d*) comparisons of the interface concentration C_s, the dissolution flux F and the volume-averaged concentration $\overline{\overline{C}}$ between the DNS results (solid lines) and the mathematical models (dashed lines). The dynamical regimes are delineated as in figure 5. In the quasi-steady convective regime, the rescaled dissolution flux keeps constant in time and is independent of Π, i.e. $F/C_s^2 = \alpha Ra_0$, where $\alpha = 0.0168$. In (*b–d*), the dots mark the time of transition to the shut-down regime from DNS for various Π. Obviously, this transition is delayed with increasing Π.

Moreover, from (2.17) the total amount dissolved is given by

$$\overline{\overline{C}}(t_a) = \frac{\alpha t_a}{\alpha \Pi t_a + 1}. \tag{4.6}$$

As shown in figure 9(*b–d*), comparisons of the mathematical models in (4.5) and (4.6) and the DNS results show good agreement in the quasi-steady convective regime, for $\Pi \leqslant 10$. In addition, the assumption that $w_d \sim C$ can be confirmed by fitting the data in figure 6(*c*) with an expression of the form (4.5*a*), to show that $w_d = C_s/8.1$. Similarly, it can be shown that $\delta \sim 1/C_s$ in figure 6(*b*). It should be noted that these are quantities measured near the interface and appropriate prefactors vary with distance from the interface.

For $\Pi = 0$, the fingertip sinks with a nearly constant speed in the quasi-steady convective regime (Riaz *et al.* 2006; Hewitt *et al.* 2013; Slim 2014). However, for $\Pi > 0$, the downward propagation velocity, w_d, slows down as the interface concentration, C_s, declines. This delays the transitions from the quasi-steady to the

https://doi.org/10.1017/jfm.2018.622 Published online by Cambridge University Press

shut-down regime, as shown in figures 6(*c*) and 9(*c*). However, since $w_d \sim C_s$ and the decline of $C_s(t)$ is determined by (4.5*a*), the fingertip position of the descending plumes is given by

$$z_{tip}(t_a) = -\int_0^{t_a} w_d \, \mathrm{d}\tilde{t}_c = -\frac{\ln(1+\alpha\Pi t_a)}{7.2\,\alpha\Pi}. \tag{4.7}$$

Here $w_d = C_s/7.2$, as in our simulations the fingers reach the lower boundary at $t_a \approx 7.2$ for $\Pi = 0$. According to the model, in closed systems the fingers first hit the base of the domain at

$$t_b = \frac{\mathrm{e}^{7.2\,\alpha\Pi} - 1}{\alpha\Pi}, \tag{4.8}$$

when $z_{tip}(t_b) = -1$. After reaching the base of the domain, dense fluid is carried upward by the return flow and, once the saturated fluid reaches the interface, convection shuts down rapidly. Due to the symmetry of the downwelling and upwelling regions (see figure 7), mass balance requires that the magnitude of horizontal-mean upwelling velocity is equal to the magnitude of horizontal-mean downwelling velocity at any time, $w_u \approx w_d$. Therefore, one might expect the time required for the transition to shut-down, t_s, to be given by solving $z_{tip}(t_b) = -2$. However, even for $\Pi = 0$ this simple estimate is not accurate and we prefer the expression

$$t_s = \frac{\mathrm{e}^{16\,\alpha_u\,\Pi} - 1}{\alpha_u\,\Pi}, \tag{4.9}$$

where $w_d = C_s/8$ has been used and $\alpha_u = 0.8\,\alpha$. These corrections account for delays due to accumulation of dense fluid at the base and for an apparent reduction of the efficiency of the return flux relative to (4.2) and (4.4). As shown in figure 10, the estimates for the time scales given by (4.8) and (4.9) agree very well with the DNS results, as long as $\Pi \leqslant 5$. At large Π, e.g. $\Pi = 10$, however, the theoretical predictions of t_b and t_s underestimate the time scales determined from the simulations. This is due to the formation of a stable density stratification at the base of the domain, shown in figure 8(*c*).

For simulations with $\Pi \leqslant 5$, the horizontal-mean concentration $\overline{C}$ exhibits a vertically well-mixed structure in the shut-down regime (see figure 8). Therefore, from the definitions in (2.15) and (2.16) and the approximation in (4.1), the dissolution flux of CO_2 can be rewritten as

$$F = \frac{\mathrm{d}}{\mathrm{d}t}\int_{-1}^{0} \overline{C}\,\mathrm{d}z = \frac{\mathrm{d}\overline{\overline{C}}}{\mathrm{d}t}. \tag{4.10}$$

As in Hewitt *et al.* (2013), we define a time-dependent Nusselt number by scaling the flux $F(t)$ up to a unit concentration difference:

$$Nu(t) = \frac{F}{C_s - \overline{\overline{C}}}, \tag{4.11}$$

where Nu varies as a function of current Rayleigh number, i.e. $Nu(t) = \mathcal{N}(Ra(t))$. Note that for $\Pi > 0$, C_s also varies as a function of time. Analogous to high-Ra Rayleigh–Bénard convection in porous media, where the Nusselt number Nu_{RB} linearly depends

https://doi.org/10.1017/jfm.2018.622 Published online by Cambridge University Press

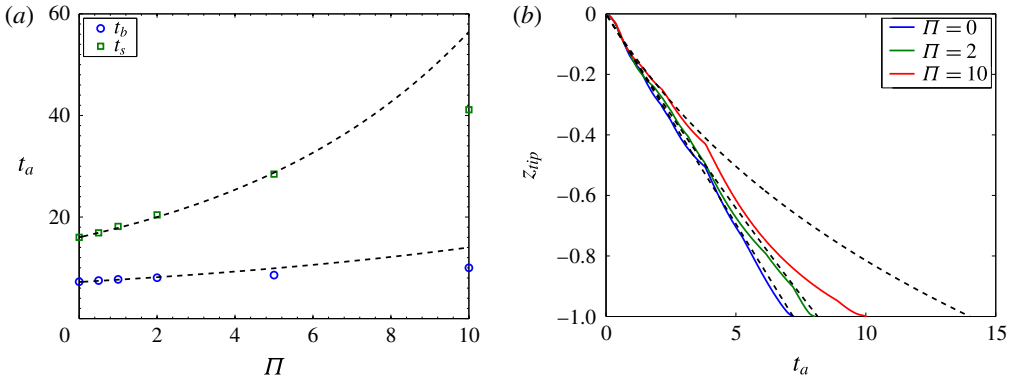


FIGURE 10. (Colour online) Measures of finger motions at $Ra_0 = 20\,000$ for different Π: (*a*) variations of t_b and t_s with Π; (*b*) evolution of the fingertip location z_{tip} in time. Symbols and solid lines, DNS results; dashed lines, mathematical models. In (*b*), the fingertip location is defined as the minima of the $C = 0.05$ contour.

on a relative Rayleigh number, the Nusselt number $Nu(t)$ in the solutal convection problem can be expressed as

$$Nu(Ra(t)) = Nu_{RB}(Ra_e) = \gamma Ra_e, \tag{4.12}$$

where the effective Rayleigh number

$$Ra_e = \chi(C_s - \overline{\overline{C}})Ra_0, \tag{4.13}$$

and γ and χ are two constant numbers. In the convection-time framework, combining (4.10)–(4.13) with (2.17) results in

$$\frac{\mathrm{d}\overline{\overline{C}}}{\mathrm{d}t_a} = \gamma\chi[1 - (1+\Pi)\overline{\overline{C}}]^2. \tag{4.14}$$

Solving this ordinary differential equation gives

$$\overline{\overline{C}}(t_a) = \frac{1}{1+\Pi}\left[1 - \frac{1}{\gamma\chi(1+\Pi)t_a + c_0}\right]. \tag{4.15}$$

From (2.17) and (4.10), we obtain the models for C_s and F for the shut-down regime:

$$C_s(t_a) = \frac{1}{1+\Pi}\left[1 + \frac{\Pi}{\gamma\chi(1+\Pi)t_a + c_0}\right] \quad \text{and} \quad F(t_a) = \frac{\gamma\chi Ra_0}{[\gamma\chi(1+\Pi)t_a + c_0]^2}. \tag{4.16a,b}$$

We choose $\gamma\chi = 0.0317$ and $c_0 = 0.861$ by fitting (4.16) with the DNS data so that, at $\Pi = 0$, our model is consistent with the theoretical box model given by Slim (2014) and $F(t_a = 16) = \alpha Ra_0$.

Figure 11 shows the comparisons between the mathematical models and the numerical simulations in the shut-down regime for different Π at $Ra_0 = 20\,000$.

https://doi.org/10.1017/jfm.2018.622 Published online by Cambridge University Press

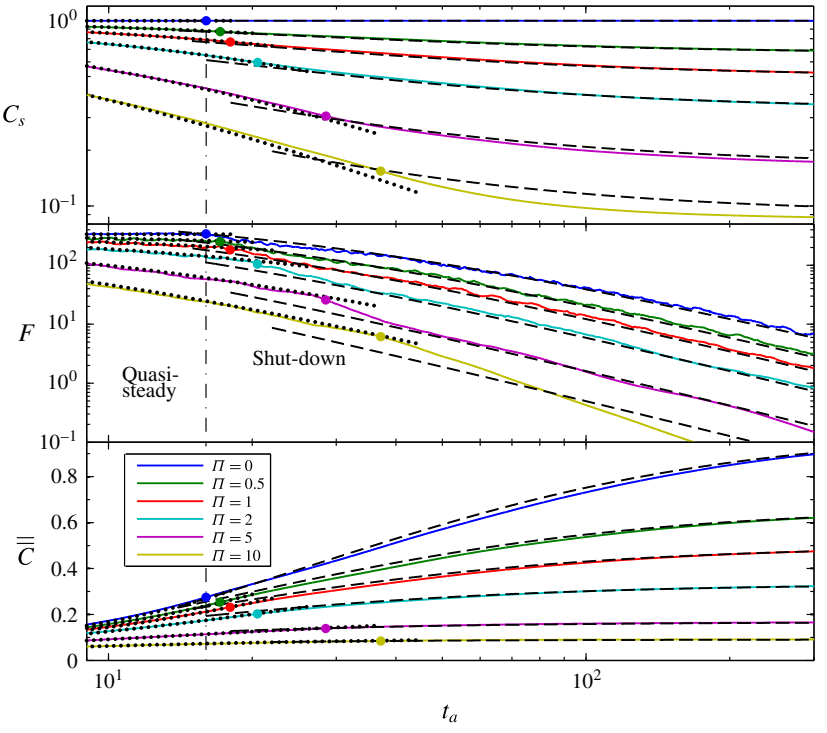


FIGURE 11. (Colour online) Comparisons between mathematical models (dashed lines) and numerical simulations (solid lines) for the shut-down regime in closed systems at $Ra_0 = 20\,000$: (*a*) the interface concentration C_s; (*b*) the dissolution flux F; (*c*) the volume-averaged concentration $\overline{\overline{C}}$. The dots mark the time of transition to the shut-down regime from DNS for various Π. For reference, mathematical models for the quasi-steady regime (dotted lines) are also plotted.

For $\Pi < 10$, the models in (4.15) and (4.16) are in good agreement with the DNS results in the shut-down regime. For $\Pi \geqslant 10$, however, the model breaks down in the shut-down regime, because a stable stratification forms at the base of the domain. Nevertheless, in these cases the water is already 95 % saturated, so that the additional dissolution during the shut-down regime is negligible. In these cases, the drop in C_s, and hence in Ra_e, is so rapid that convection is not vigorous enough to maintain a well-mixed solution near the bottom.

To verify the mathematical models developed above, DNS were also performed for other high Rayleigh numbers following the same strategy described at the beginning of § 4, but using different numbers of vertical modes and time steps. Figure 12 compares the mathematical models with the DNS results in different flow regimes at $\Pi = 2$ for $Ra_0 = 10\,000$, $20\,000$ and $50\,000$. The models (4.5), (4.9) and (4.16) match well with the simulation results for various Ra_0 due to the asymptotic high-Rayleigh-number behaviour of convection in porous media. Moreover, for fixed Π our DNS results indeed show that the rescaled dissolution flux $\widetilde{F}$, the time of transition to the shut-down regime t_s, and the interface concentration C_s are independent of Ra_0 in terms of advection time in both quasi-steady and shut-down regimes, as also revealed from the models.

https://doi.org/10.1017/jfm.2018.622 Published online by Cambridge University Press

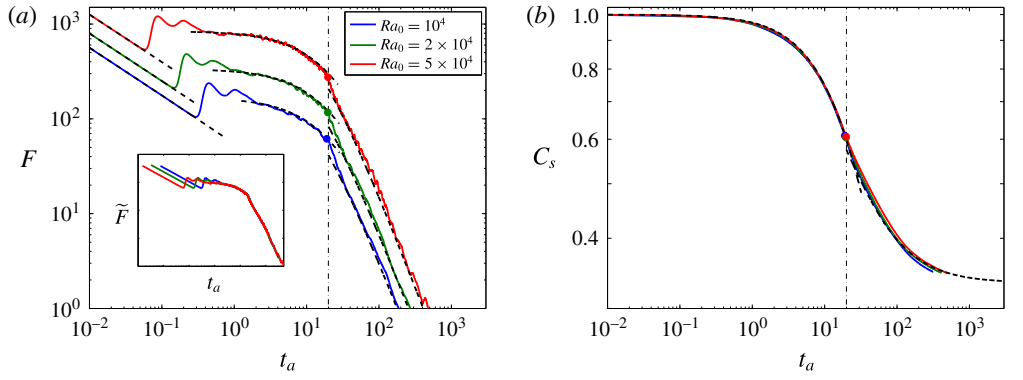


FIGURE 12. (Colour online) Comparisons between mathematical models (dashed lines) and numerical simulations (solid lines) at $\Pi = 2$ for various Ra_0: (*a*) the dissolution flux F; (*b*) the interface concentration C_s. The inset in (*a*) shows the evolution of normalised flux $\widetilde{F} = F/(\alpha Ra_0)$ in time, and the dots and dot-dashed lines mark the time of transition to the shut-down regime from DNS and the model (4.9), respectively.

Although our models in this manuscript only focus on 2D domains, the study by Shi *et al.* (2018) reveals that a similar 2D convective modelling strategy predicts the dissolution rate of CO_2 at initial pressures up to 6 MPa at $T = 50\,^{\circ}\mathrm{C}$ in a 3D cylinder filled with water-saturated porous media. Moreover, investigations by Pau *et al.* (2010), Fu, Cueto-Felgueroso & Juanes (2013) and Hewitt, Neufeld & Lister (2014) indicate that the power-law-scaling characteristics appearing in 2D also exist in 3D buoyancy-driven porous media convection. Therefore, it is possible to apply our 2D mathematical models directly to 3D or extend the 2D models to 3D by changing appropriate coefficients.

5. Discussion

The pressure drop induced by CO_2 dissolution in a closed reservoir provides a strong negative feedback for convective dissolution. While engineered storage sites are likely open systems to limit pressure build-up during injection, natural CO_2 reservoirs may be closed systems. Understanding the dynamics of natural CO_2 accumulations is important, since they are our only analogues for the long-term fate of geological CO_2 storage.

In the analyses presented below it should be kept in mind that the models presented here are based on numerous assumptions. Most importantly, our results are based on simulations in two-dimensional homogeneous isotropic systems with rectangular geometry, and they neglect hydrodynamic dispersion.

5.1. *Closed system dissolution in the Bravo Dome natural* CO_2 *field*

The Bravo Dome CO_2 field in New Mexico is commonly used as an analogue for geological CO_2 storage, but recent work has shown that it comprises a number of isolated pressure compartments (Akhbari & Hesse 2017). It is unclear when these compartments became isolated and started acting as closed systems. In the calculation below we assume that they have been isolated for the majority of the lifetime of the reservoir. Here we focus on the NE section of the reservoir, where significant

https://doi.org/10.1017/jfm.2018.622 Published online by Cambridge University Press

CO_2 dissolution has occurred (Gilfillan *et al.* 2009; Sathaye *et al.* 2014). This section is separated from the main reservoir by a major fault and parts of it are underlaid by a deep aquifer. In this section, the dissolution capacity is $\Pi \approx 2$, the average depth of the reservoir is $H_w = 130$ m, the vertical permeability $K = 2.5 \times 10^{-15}$ m^2, the porosity $\varphi = 0.14$, the tortuosity of sandstone is $\tau \approx 4$, gravitational acceleration $g = 9.8$ m s^{-2}, initial density difference $\Delta\rho_0^* = 10.5$ kg m^{-3}, water viscosity at 35 °C is $\mu = 8.9 \times 10^{-4}$ Pa s, and the diffusivity of aqueous CO_2 is $D_m = 2 \times 10^{-9}$ m^2 s^{-1}.

Due to the relatively large tortuosity the effective diffusivity, $D = D_m/\tau$, in the sandstones is only 5×10^{-10} m^2 s^{-1} and may be even less in the lower porosity siltstones (Gist *et al.* 1990; Hürlimann *et al.* 1994; Zecca *et al.* 2016). The resulting initial Rayleigh number in this field is $Ra_0 \approx 540$ and the characteristic time scales are $\mathcal{T}_{ad} \approx 4$ years, $\mathcal{T}_a \approx 2000$ years and $\mathcal{T}_d \approx 1$ Ma. Although the Rayleigh number is large enough that Bravo Dome likely experienced convective CO_2 dissolution, it was not vigorous enough for a well-developed quasi-steady convection regime, so that the models developed in § 4.2 do not apply to Bravo Dome.

Instead, the diffusive models developed in § 3.1 provide an upper bound on the dissolution time scales at Bravo Dome. The time required for dissolved CO_2 to diffuse to the bottom of the reservoir is $t_d \approx 0.1\mathcal{T}_d$, which corresponds to approximately 100 000 years in the NE section of Bravo Dome. The time required to saturate the underlying aquifer is $t_d \approx \mathcal{T}_d$ (figure 3*d*) and hence comparable to the estimated lifetime of the reservoir (Sathaye *et al.* 2014). This calculation assumes that all brine directly underlies the gas–water interface. In the NE section of Bravo Dome this is not strictly true, since the gas is localised within two domes and significant lateral transport has to occur to saturate the entire brine within the reservoir.

In the context of the simplified model explored here; however, it is possible that the underlying brine has been saturated. In this case, the fraction of CO_2 that has been dissolved at global equilibrium is given by

$$\frac{P^*_{g,0} - P^*_{g,e}}{P^*_{g,0}} = 1 - C_{s,e} = \frac{\Pi}{1+\Pi} \approx 0.66. \tag{5.1}$$

The maximum amount of dissolution in the NE segment of Bravo Dome is limited to two-thirds of the amount that would have occurred in an equivalent open system. This is due to the significant drop in the gas pressure, which lowers the aqueous solubility of CO_2. The theoretical estimate (5.1) is comparable to the estimate of 0.5, based on noble gases and reservoir characterisation (Sathaye *et al.* 2014).

To more comprehensively understand the convective CO_2 dissolution process in Bravo Dome, DNS were also performed at $Ra_0 = 540$ for various Π. It is seen from figure 13 that the CO_2 dissolution is significantly affected by Π at moderate Ra_0: the onset time is delayed as Π increases and at $\Pi \gtrsim 10$ no convection occurs, i.e. the transport is by diffusion. Based on these DNS data, for $\Pi = 0$ convection sets in after $130\,\mathcal{T}_{ad} \approx 480$ years and the dissolution flux starts to grow after $3000\,\mathcal{T}_{ad} \approx 11\,000$ years; while for $\Pi = 2$, the onset of convection occurs around $140\,\mathcal{T}_{ad} \approx 520$ years and the dissolution flux starts to grow after $4300\,\mathcal{T}_{ad} \approx 16\,000$ years. Moreover, figure 13 also reveals that no apparent quasi-steady convective regime exists at $Ra_0 = 540$, e.g. for $\Pi \leqslant 5$ the convection begins to shut down right after the flux-growth and plume-merging regime. For $\Pi = 0$, the dissolution flux is halved after 70 000 years and is one-tenth of its initial value after 200 000 years; and the reservoir becomes 95 % saturated after 420 000 years. For $\Pi > 0$, however, the dissolution flux declines significantly due to the negative feedback of

https://doi.org/10.1017/jfm.2018.622 Published online by Cambridge University Press

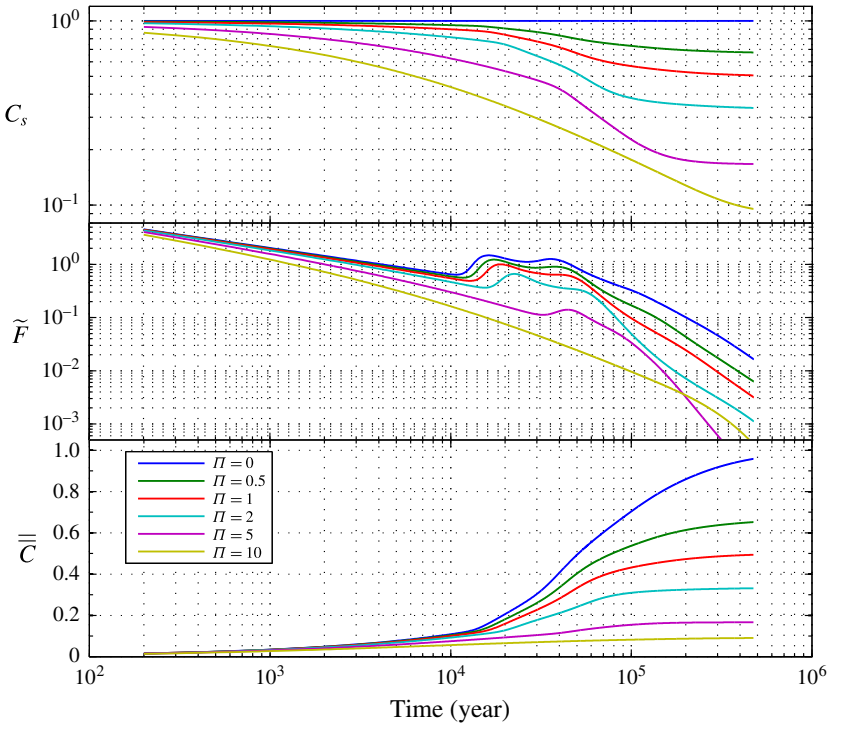


FIGURE 13. (Colour online) Evolution of the interface concentration C_s, the normalised dissolution flux $\widetilde{F} = F/(\alpha Ra_0)$ and the total dissolution $\overline{\overline{C}}$ in dimensional time for $Ra_0 = 540$, based on the Bravo Dome field parameters. The domain aspect ratio for the DNS reported here is $L = 10^5/Ra_0 \approx 185$.

pressure drop in the gas field: compared with $\Pi = 0$, the dissolution flux for $\Pi = 2$ is halved after 29 000 years with gas pressure reduced to 65 % and becomes one-tenth after 82 000 years with gas pressure reduced to 40 %; and the reservoir becomes 95 % saturated after 130 000 years. The closed system with $\Pi > 0$ therefore saturates earlier than that with $\Pi = 0$, but the total amount dissolved is less due to the drop in gas pressure. When comparing these estimates the simplifications in the model and the large uncertainties in the interpretation of the field data should be kept in mind.

5.2. *Time scales of high-Rayleigh-number convection in closed system*

To illustrate the effect of a closed system on a vigorously convecting system, we apply the high-Ra_0 convection models developed in § 4.2 to a hypothetical closed, high-permeability reservoir used in previous work (Neufeld *et al.* 2010; Hewitt *et al.* 2013). The parameters $H_w = 20$ m, $K = 2.5 \times 10^{-12}$ m^2, $\Delta\rho_0^* = 10.5$ kg m^{-3}, $\varphi = 0.375$, $D_m = 2 \times 10^{-9}$ m^2 s^{-1} and $\mu = 5.9 \times 10^{-4}$ Pa s are loosely based on the Sleipner site in North Sea (Bickle *et al.* 2007; Pau *et al.* 2010). This reservoir comprises unconsolidated sand, so that $\tau \approx \sqrt{2}$ and the effective diffusivity is $D = D_m/\tau \approx 1.4 \times 10^{-9}$. The resulting initial Rayleigh number is $Ra_0 \approx 1.6 \times 10^4$, and the characteristic time scales are $\mathcal{T}_{ad} \approx 0.3$ h, $\mathcal{T}_a \approx 0.5$ years and $\mathcal{T}_d \approx 9000$ years. As discussed in §§ 3.2 and 4.1, the dynamics in the diffusion-dominant regime are generally not affected by Π at large Ra_0. Therefore, in such closed aquifers,

https://doi.org/10.1017/jfm.2018.622 Published online by Cambridge University Press

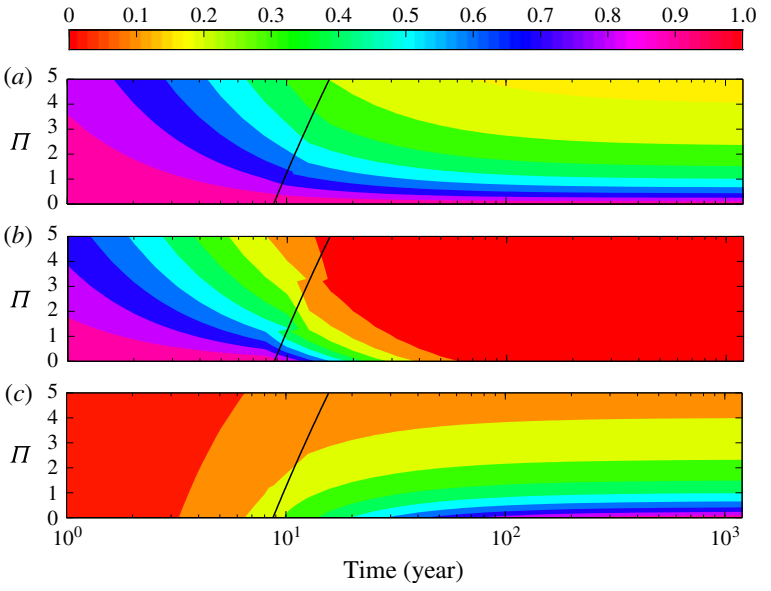


FIGURE 14. (Colour online) Contours of (*a*) the normalised gas pressure, $\widetilde{P} = P_g^*/P_{g,0}^* = C_s$, (*b*) the normalised dissolution flux, $\widetilde{F} = F/(\alpha Ra_0)$, and (*c*) the total dissolution $\overline{\overline{C}}$, based on the box models developed in § 4.2, for the high-permeability reservoir. The solid line marks the dimensional shut-down time $t_s^* = t_s \mathcal{T}_a$ based on (4.9). The zigzag contours around $t^* = t_s^*$ are due to the discontinuities of the box models for the quasi-steady convective and shut-down regimes at t_s.

convection sets in after $130\,\mathcal{T}_{ad} \approx 2$ days and the dissolution flux starts to grow after $3000\,\mathcal{T}_{ad} \approx 36$ days.

To exhibit the long-term effect of the parameter Π on CO_2 dissolution, we estimate the evolution of the normalised gas pressure $P_g^*/P_{g,0}^*$ (i.e. C_s), dissolution flux $F/(\alpha Ra_0)$ and total dissolved CO_2 (i.e. $\overline{\overline{C}}$) in time for this high-permeability reservoir using the box models developed in § 4.2. As shown in figure 14, for $\Pi = 0$ the convection starts to shut down after nine years; the dissolution flux is halved after 19 years and is one-tenth of its initial value after 60 years; and the reservoir becomes 95 % saturated after 330 years. For $\Pi = 2$, however, the pressure in the gas field declines significantly as CO_2 dissolves into the water: the convection shuts down after 11 years, when the gas pressure is reduced to 57 % of its initial value. Due to this negative feedback, the dissolution flux is halved after seven years and is one-tenth of its initial value after 20 years, and the reservoir becomes 95 % saturated after 110 years.

6. Conclusions

We have examined the dynamics of convective CO_2 dissolution in a closed porous media system, where the dissolution is accompanied by a drop in gas pressure. This introduces a negative feedback that slows both diffusive and convective mass transport and reduces the overall amount of CO_2 that can be dissolved. The strength of this negative feedback is controlled by the dimensionless dissolution capacity, Π, which corresponds to the fraction of the initial gas that can be dissolved into the water

https://doi.org/10.1017/jfm.2018.622 Published online by Cambridge University Press

at equilibrium. The dynamics in a closed system with $\Pi > 0$ differ fundamentally from the previous common studies with $\Pi = 0$, since the interface concentration, which drives mass transport, declines with time. For $\Pi > 0$, diffusive mass transport is no longer self-similar and convective mass transport is never quasi-steady with a constant flux. However, we use DNS to show that the flux F is quadratic in the interface concentration C_s at high Rayleigh numbers. This allows the construction of box models that successfully capture the mean behaviour of the convecting system. Our results show that the pressure drop in closed systems can significantly limit convection long before the underlying brine begins to saturate. This may explain the persistence of natural CO_2 accumulations in isolated reservoir compartments over geological time periods.

As discussed earlier, our models, analysis and numerical simulations in this manuscript are based on many assumptions, including ideal-gas law, invariant volume of water during CO_2 dissolution, homogeneous isotropic systems, and negligible hydrodynamic dispersion, etc. These limitations should be kept in mind when the readers try to apply the analysis and models to other CO_2–water dissolution systems and specific reservoirs. In Shi *et al.* (2018), however, we have successfully applied the modelling strategies reported here to real-gas cases ($P^*_{g,0} \approx 6$ MPa) by adding a P^*_g-dependent compressibility factor, $Z(P^*_g)$, in the equation of state (1.1) and considering a P^*_g-dependent solubility, $K_h(P^*_g)$, in the Henry's law equation (1.2), where Z and K_h are fitted to previously published batch phase equilibrium data. Moreover, the study by Shi *et al.* (2018) and the discussion in the appendix also reveal that the change in the aqueous-phase volume due to CO_2 dissolution is still negligible (less than 3 %) at $P^*_{g,0} = 7$ MPa and $T = 50\,^{\circ}\mathrm{C}$, implying that in the modelling of convection the constant-water-volume assumption is applicable to most current laboratory experiments mentioned in this paper and many underpressured natural CO_2 reservoirs listed in Miocic *et al.* (2016) and Akhbari & Hesse (2017), where CO_2 behaves as a real gas. Nevertheless, above a certain high-pressure criterion, the large solubility of CO_2 in water will lead to a non-negligible increase of the aqueous-phase volume, and thereby might have a first-order effect on the convective process in closed porous media systems (Moortgat 2018).

Acknowledgements

We thank Dr K. Jessen for providing experimental data. This work was supported as part of the Center for Frontiers in Subsurface Energy Security, an Energy Frontier Research Center funded by the US Department of Energy, Office of Science, Basic Energy Sciences under Award no. DE-SC0001114. B.W. acknowledges the Peter O'Donnell, Jr. Postdoctoral Fellowship through the Institute of Computational and Engineering and Science at the University of Texas at Austin.

Appendix A. Volume change of aqueous phase due to CO_2 dissolution

In this appendix, we evaluate the volume change of the aqueous phase due to CO_2 dissolution, based on available literature data and models of the CO_2 solubility in water and the saturated aqueous-phase density. For a given amount of water V^*_w at a certain temperature, we consider the case of $\Pi = 0$ in the closed system, i.e. $V^*_g \to \infty$, so that the gas pressure P^*_g remains constant during equilibration, and the magnitude of CO_2 dissolution reaches the maximum compared with other cases ($\Pi > 0$).

At equilibrium (i.e. $t^* \to \infty$), the total mass of CO_2 dissolved in the aqueous phase is

$$M^*_{\mathrm{CO}_2,a} = \Omega C^*_s V^*_{a,e}, \tag{A 1}$$

https://doi.org/10.1017/jfm.2018.622 Published online by Cambridge University Press

where $\Omega = 0.044$ kg mol^{-1} is the molecular weight of CO_2, C_s^* is the solubility of CO_2 in the aqueous phase (i.e. the concentration of CO_2 in the solution), and $V_{a,e}^*$ is the volume of the saturated aqueous phase. In general, C_s^* is a nonlinear function of P_g^* and its functional form can be obtained from previously published batch phase equilibrium data or models. Then, the total mass of the aqueous phase at global equilibrium is

$$M_{a,e}^* = M_{H_2O,0}^* + M_{CO_2,a}^* = \rho_{H_2O,0}^* V_w^* + \Omega C_s^* V_{a,e}^*, \tag{A 2}$$

where $M_{H_2O,0}^*$ and $\rho_{H_2O,0}^*$ are the mass and the density of fresh water, respectively. Since $V_{a,e}^* = M_{a,e}^*/\rho_{a,e}^*$, from (A 2) the volume of the aqueous phase after CO_2 dissolution can be expressed as

$$V_{a,e}^* = \frac{\rho_{H_2O,0}^* V_w^*}{\rho_{a,e}^* - \Omega C_s^*} = \frac{\rho_{H_2O,0}^* V_w^*}{\rho_{H_2O,0}^* + \Delta\rho^* - \Omega C_s^*}, \tag{A 3}$$

where the density of the aqueous phase, $\rho_{a,e}^*$, or the density difference between the fresh water and the saturated water, $\Delta\rho^*$, can be also obtained from previously published batch phase equilibrium data or models. Therefore, the relative volume change of the aqueous phase due to CO_2 dissolution is

$$\Lambda = \frac{V_{a,e}^* - V_w^*}{V_w^*} = \frac{\rho_{H_2O,0}^*}{\rho_{H_2O,0}^* + \Delta\rho^* - \Omega C_s^*} - 1. \tag{A 4}$$

Below we quantify Λ using the literature data and models of C_s^* and $\Delta\rho^*$ from Duan & Sun (2003), Efika *et al.* (2016), Shi *et al.* (2018) at $T = 50\,^{\circ}$C. As shown in figure 15, the volume of the aqueous phase increases monotonically as a function of the gas pressure P_g^*. For $P_g^* \lesssim 1$ MPa, CO_2 can be treated approximately as an ideal gas, and both the solubility C_s^* and the density change $\Delta\rho^*$ increase linearly with P_g^*, i.e. $C_s^* = 178.140 P_g^*$ and $\Delta\rho^* = 2.145 P_g^*$. Hence, from (A 4), $\Lambda = 988/(988 - 5.693 P_g^*) - 1$, e.g. $\Lambda = 0.58\,\%$ at $P_g^* = 1$ MPa. For $P_g^* > 1$ MPa, CO_2 deviates from the ideal-gas state, and both C_s^* and $\Delta\rho^*$ change as quadratic functions of P_g^*. Therefore the relative volume change of the aqueous phase, Λ, due to CO_2 dissolution is approximately 3 % at $P_g^* = 7$ MPa and 3.5 % at $P_g^* = 12$ MPa. This justifies our assumption that the volume change is small for the pressures encountered in underpressured natural CO_2 reservoirs, such as Bravo Dome.

Further we note that under real reservoir conditions, the CO_2 solubility in brine is generally less than that in pure water (Duan & Sun 2003; Mao *et al.* 2013; Jacob & Saylor 2016; Shi *et al.* 2018), and in closed systems with $\Pi > 0$, the drop of the gas pressure will further reduce the amount of CO_2 dissolved into the aqueous phase and hence the change in water volume. Both of these factors may increase the pressure criterion below which the change of the aqueous-phase volume can be ignored. In any case, within the scope of this study, i.e. the low-pressure regime, the volume change of the aqueous phase is negligible.

The above analysis does not imply, of course, the volume change of the aqueous phase due to CO_2 dissolution can be neglected in measuring or modelling the solubility C_s^* and the density change $\Delta\rho^*$. In both Shi *et al.* (2018) and this study, we just neglect the volume change in the modelling of convection, but use the $C_s^*(P_g^*)$ and $\Delta\rho^*(P_g^*)$ functions directly from experimental measurements or models at given pressure and temperature (see figure 15) that have naturally considered the variation

https://doi.org/10.1017/jfm.2018.622 Published online by Cambridge University Press

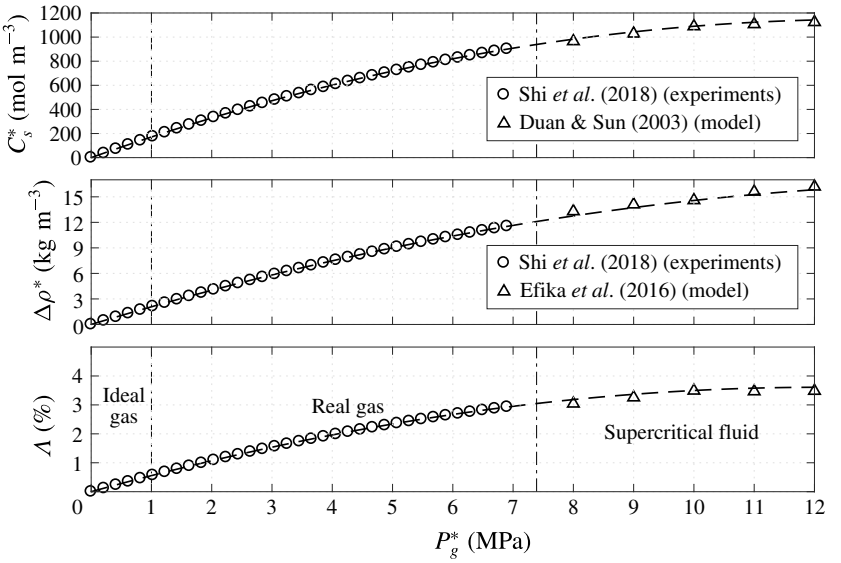


FIGURE 15. Variation of the CO_2 solubility C_s^*, the density change $\Delta\rho^*$ and the volume change Λ in the aqueous phase, as a function of the gas pressure P_g^* at $T = 50\,^{\circ}\mathrm{C}$. The experimental data of Shi *et al.* (2018) for C_s^* and $\Delta\rho^*$ are shown as circles, while previous model results by Duan & Sun (2003) and Efika *et al.* (2016) under supercritical conditions are shown as triangles. We note that the symbols shown for Λ are calculated from the data for C_s^* and $\Delta\rho^*$ using (A 4). We fit quadratic polynomials to the experimental data of C_s^* and $\Delta\rho^*$ at $P_g^* \leqslant 7$ MPa, i.e. $C_s^* = -6.916P_g^{*2} + 178.140P_g^*$ and $\Delta\rho^* = -0.0687P_g^{*2} + 2.145P_g^*$ (dashed lines), and thereby obtain $\Lambda = 988/(0.236P_g^{*2} - 5.693P_g^* + 988) - 1$ (dashed line). These fits to the gaseous data also approximate the supercritical behaviour reasonably well.

of the aqueous-phase volume. This will introduce a relative error, with the magnitude $\sim O(\Lambda)$, for the total amount of CO_2 dissolved into water at the global equilibrium.

REFERENCES

AKHBARI, D. & HESSE, M. A. 2017 Causes of underpressure in natural CO_2 reservoirs and implications for geological storage. *Geology* **45**, 47–50.

AZIN, R., MAHMOUDY, M., RAAD, S. M. J. & OSFOURI, S. 2013 Measurement and modeling of CO_2 diffusion coefficient in saline aquifer at reservoir conditions. *Cent. Eur. J. Engng* **3**, 585–594.

BACKHAUS, S., TURITSYN, K. & ECKE, R. E. 2011 Convective instability and mass transport of diffusion layers in a Hele-Shaw geometry. *Phys. Rev. Lett.* **106**, 104501.

BARLETTA, A. & STORESLETTEN, L. 2012 Onset of convection in a porous rectangular channel with external heat transfer to upper and lower fluid environments. *Trans. Porous Med.* **94**, 659–681.

BARLETTA, A., TYVAND, P. A. & NYGØARD, H. S. 2015 Onset of thermal convection in a porous layer with mixed boundary conditions. *J. Engng Maths* **91**, 105–120.

BICKLE, M., CHADWICK, A., HUPPERT, H. E., HALLWORTH, M. & LYLE, S. 2007 Modelling carbon dioxide accumulation at Sleipner: implications for underground carbon storage. *Earth Planet. Sci. Lett.* **255**, 164–176.

https://doi.org/10.1017/jfm.2018.622 Published online by Cambridge University Press

BOYD, J. P. 2000 *Chebyshev and Fourier Spectral Methods*, 2nd edn. Dover.

BROADHEAD, R. F. 1987 Carbon dioxide in Union and Harding counties. In *New Mexico Geological Society Guidebook, 38th Field Conference*, pp. 339–349. New Mexico Geological Society.

BROADHEAD, R. F. 1990 *Structural Traps I: Tectonic Fold Traps*. American Association of Petroleum Geologists.

CRANK, J. 1975 *The Mathematics of Diffusion*, 2nd edn. Oxford University Press.

DOERING, C. R. & CONSTANTIN, P. 1998 Bounds for heat transport in a porous layer. *J. Fluid Mech.* **376**, 263–296.

DUAN, Z. & SUN, R. 2003 An improved model calculating CO_2 solubility in pure water and aqueous NaCl solutions from 273 to 533 K and from 0 to 2000 bar. *Chem. Geol.* **193**, 257–271.

DUFFY, D. G. 2004 *Transform Methods for Solving Partial Differential Equations*, 2nd edn. Chapman & Hall/CRC.

EFIKA, E. C., HOBALLAH, R., LI, X., MAY, E. F., NANIA, M., SANCHEZ-VICENTE, Y. & TRUSLER, J. P. M. 2016 Saturated phase densities of $(CO_2 + H_2O)$ at temperatures from (293 to 450) K and pressures up to 64 MPa. *J. Chem. Thermodyn.* **93**, 347–359.

ELENIUS, M. T. & JOHANNSEN, K. 2012 On the time scales of nonlinear instability in miscible displacement porous media flow. *Comput. Geosci.* **16**, 901–911.

ELENIUS, M. T., NORDBOTTEN, J. M. & KALISCH, H. 2014 Convective mixing influenced by the capillary transition zone. *Comput. Geosci.* **18**, 417–431.

EMAMI-MEYBODI, H., HASSANZADEH, H., GREEN, C. P. & ENNIS-KING, J. 2015 Convective dissolution of CO_2 in saline aquifers: progress in modeling and experiments. *Intl J. Greenh. Gas Control* **40**, 238–266.

ENNIS-KING, J., PRESTON, I. & PATERSON, L. 2005 Onset of convection in anisotropic porous media subject to a rapid change in boundary conditions. *Phys. Fluids* **17**, 084107.

FARAJZADEH, R., ZITHA, P. L. J. & BRUINING, J. 2007 Mass transfer of CO_2 into water and surfactant solutions. *Petrol. Sci. Technol.* **25**, 1493–1511.

FARAJZADEH, R., ZITHA, P. L. J. & BRUINING, J. 2009 Enhanced mass transfer of CO_2 into water: Experiment and modeling. *Ind. Engng Chem. Res.* **48**, 6423–6431.

FU, X., CUETO-FELGUEROSO, L. & JUANES, R. 2013 Pattern formation and coarsening dynamics in three-dimensional convective mixing in porous media. *Phil. Trans. R. Soc. Lond.* A **371**, 20120355.

GILFILLAN, S. M. V., BALLENTINE, C. J., HOLLAND, G., BLAGBURN, D., LOLLAR, B. S., STEVENS, S., SCHOELL, M. & CASSIDY, M. 2008 The noble gas geochemistry of natural CO_2 gas reservoirs from the Colorado Plateau and Rocky Mountain provinces, USA. *Geochim. Cosmochim. Acta* **72**, 1174–1198.

GILFILLAN, S. M. V., LOLLAR, B. S., HOLLAND, G., BLAGBURN, D., STEVENS, S., SCHOELL, M., CASSIDY, M., DING, Z., ZHOU, Z., LACRAMPE-COULOUME, G. & BALLENTINE, C. J. 2009 Solubility trapping in formation water as dominant CO_2 sink in natural gas fields. *Nature* **458**, 614–618.

GIST, G. A., THOMPSON, A. H., KATZ, A. J. & HIGGINS, R. L. 1990 Hydrodynamic dispersion and pore geometry in consolidated rock. *Phys. Fluids* A **2**, 1533–1544.

GOLDING, M. J., NEUFELD, J. A., HESSE, M. A. & HUPPERT, H. E. 2011 Two-phase gravity currents in porous media. *J. Fluid Mech.* **678**, 248–270.

HASSANZADEH, H., POOLADI-DARVISH, M. & KEITH, D. W. 2006 Stability of a fluid in a horizontal saturated porous layer: effect of non-linear concentration profile, initial, and boundary conditions. *Trans. Porous Med.* **65**, 193–211.

HASSANZADEH, P., CHINI, G. P. & DOERING, C. R. 2014 Wall to wall optimal transport. *J. Fluid Mech.* **751**, 627–662.

HEWITT, D. R., NEUFELD, J. A. & LISTER, J. R. 2012 Ultimate regime of high Rayleigh number convection in a porous medium. *Phys. Rev. Lett.* **108**, 224503.

HEWITT, D. R., NEUFELD, J. A. & LISTER, J. R. 2013 Convective shutdown in a porous medium at high Rayleigh number. *J. Fluid Mech.* **719**, 551–586.

HEWITT, D. R., NEUFELD, J. A. & LISTER, J. R. 2014 High Rayleigh number convection in a three-dimensional porous medium. *J. Fluid Mech.* **748**, 879–895.

https://doi.org/10.1017/jfm.2018.622 Published online by Cambridge University Press

HIDALGO, J. J., FE, J., CUETO-FELGUEROSO, L. & JUANES, R. 2012 Scaling of convective mixing in porous media. *Phys. Rev. Lett.* **109**, 264503.

HITCHEN, J. & WELLS, A. J. 2016 The impact of imperfect heat transfer on the convective instability of a thermal boundary layer in a porous media. *J. Fluid Mech.* **794**, 154–174.

HORTON, C. W. & ROGERS, F. T. 1945 Convection currents in a porous medium. *J. Appl. Phys.* **16**, 367–370.

HUPPERT, H. E. & NEUFELD, J. A. 2014 The fluid mechanics of carbon dioxide sequestration. *Annu. Rev. Fluid Mech.* **46**, 255–272.

HÜRLIMANN, M. D., HELMER, K. G., LATOUR, L. L. & SOTAK, C. H. 1994 Restricted diffusion in sedimentary rocks: determination of surface-area-to-volume ratio and surface relaxivity. *J. Magn. Reson* A **111**, 169–178.

JACOB, R. & SAYLOR, B. Z. 2016 CO_2 solubility in multi-component brines containing NaCl, KCl, $CaCl_2$ and $MgCl_2$ at 297 K and 1–14 MPa. *Chem. Geol.* **424**, 86–95.

JAVAHERI, M., ABEDI, J. & HASSANZADEH, H. 2010 Linear stability analysis of double-diffusive convection in porous media, with application to geological storage of CO_2. *Trans. Porous Med.* **84**, 441–456.

KIM, M. C. 2015 The effect of boundary conditions on the onset of buoyancy-driven convection in a brine-saturated porous medium. *Trans. Porous Med.* **107**, 469–487.

KIM, M. C. & CHOI, C. K. 2012 Linear stability analysis on the onset of buoyancy-driven convection in liquid-saturated porous medium. *Phys. Fluids* **24**, 044102.

KIM, M. C., SONG, K. H., CHOI, C. K. & YEO, J.-K. 2008 Onset of buoyancy-driven convection in a liquid-saturated cylindrical porous layer supported by a gas layer. *Phys. Fluids* **20**, 054104.

KIM, M. C., YOON, D. Y. & CHOI, C. K. 2006 Onset of buoyancy-driven instability in gas diffusion systems. *Ind. Engng Chem. Res.* **45**, 7321–7328.

KUBITSCHEK, J. P. & WEIDMAN, P. D. 2003 Stability of a fluid-saturated porous medium heated from below by forced convection. *Intl J. Heat Mass Transfer* **46**, 3697–3705.

LAPWOOD, E. R. 1948 Convection of a fluid in a porous medium. *Proc. Camb. Phil. Soc.* **44**, 508–521.

MA, X., ABE, Y., KANEKO, A., FUJIMOTO, S. & MURAKAMI, C. 2017 Study on dissolution process of liquid CO_2 into water under high pressure condition for CCS. *Energy Procedia* **114**, 5430–5437.

MAO, S., ZHANG, D., LI, Y. & LIU, N. 2013 An improved model for calculating CO_2 solubility in aqueous NaCl solutions and the application to CO_2–H_2O–NaCl fluid inclusions. *Chem. Geol.* **347**, 43–58.

MARTINEZ, M. J. & HESSE, M. A. 2016 Two-phase convective CO_2 dissolution in saline aquifers. *Water Resour. Res.* **52**, 585–599.

METZ, B., DAVIDSON, O., DE CONINCK, H., LOOS, M. & MEYER, L. 2005 *IPCC Special Report on Carbon Dioxide Capture and Storage*. Cambridge University Press.

MIOCIC, J. M., GILFILLAN, S. M. V., ROBERTS, J. J., EDLMANN, K., MCDERMOTT, C. I. & HASZELDINE, R. S. 2016 Controls on CO_2 storage security in natural reservoirs and implications for CO_2 storage site selection. *Intl J. Greenh. Gas Control* **51**, 118–125.

MOGHADDAM, R. N., ROSTAMI, B., POURAFSHARY, P. & FALLAHZADEH, Y. 2012 Quantification of density-driven natural convection for dissolution mechanism in CO_2 sequestration. *Trans. Porous Med.* **92**, 439–456.

MOJTABA, S., BEHZAD, R., RASOUL, N. M. & MOHAMMAD, R. 2014 Experimental study of density-driven convection effects on CO_2 dissolution rate in formation water for geological storage. *J. Nat. Gas Sci. Engng* **21**, 600–607.

MOORTGAT, J. 2018 Reservoir simulation with the cubic plus (cross-) association equation of state for water, CO_2, hydrocarbons, and tracers. *Adv. Water Resour* **114**, 29–44.

NEUFELD, J. A., HESSE, M. A., RIAZ, A., HALLWORTH, M. A., TCHELEPI, H. A. & HUPPERT, H. E. 2010 Convective dissolution of carbon dioxide in saline aquifers. *Geophys. Res. Lett.* **37**, L22404.

NIKITIN, N. 2006 Third-order-accurate semi-implicit Runge–Kutta scheme for incompressible Navier–Stokes equations. *Intl J. Numer. Meth. Fluids* **51**, 221–233.

https://doi.org/10.1017/jfm.2018.622 Published online by Cambridge University Press

ORR, F. M. 2009 Onshore geologic storage of CO_2. *Science* **325**, 1656–1658.

OTERO, J., DONTCHEVA, L. A., JOHNSTON, H., WORTHING, R. A., KURGANOV, A., PETROVA, G. & DOERING, C. R. 2004 High-Rayleigh-number convection in a fluid-saturated porous layer. *J. Fluid Mech.* **500**, 263–281.

PAOLI, M. D., ZONTA, F. & SOLDATI, A. 2016 Influence of anisotropic permeability on convection in porous media: implications for geological CO_2 sequestration. *Phys. Fluids* **28** (5), 056601.

PAOLI, M. D., ZONTA, F. & SOLDATI, A. 2017 Dissolution in anisotropic porous media: modelling convection regimes from onset to shutdown. *Phys. Fluids* **29**, 026601.

PAU, G. S. H., BELL, J. B., PRUESS, K., ALMGREN, A. S., LIJEWSKI, M. J. & ZHANG, K. 2010 High-resolution simulation and characterization of density-driven flow in CO_2 storage in saline aquifers. *Adv. Water Resour.* **33**, 443–455.

PEYRET, R. 2002 *Spectral Methods for Incompressible Viscous Flow*. Springer.

RAAD, S. M. J., AZIN, R. & OSFOURI, S. 2015 Measurement of CO_2 diffusivity in synthetic and saline aquifer solutions at reservoir conditions: the role of ion interactions. *Heat Mass Transfer* **51**, 1587–1595.

RIAZ, A. & CINAR, Y. 2014 Carbon dioxide sequestration in saline formations. Part I. Review of the modeling of solubility trapping. *J. Petrol. Sci. Engng* **124**, 367–380.

RIAZ, A., HESSE, M., TCHELEPI, H. A. & ORR, F. M. JR 2006 Onset of convection in a gravitationally unstable diffusive boundary layer in porous media. *J. Fluid Mech.* **548**, 87–111.

RIAZI, M. R. 1996 A new method for experimental measurement of diffusion coefficients in reservoir fluids. *J. Petrol. Sci. Engng* **14**, 235–250.

SATHAYE, K. J., HESSE, M. A., CASSIDY, M. & STOCKLI, D. F. 2014 Constraints on the magnitude and rate of CO_2 dissolution at Bravo Dome natural gas field. *Proc. Natl Acad. Sci. USA* **111**, 15332–15337.

SCHIFF, J. L. 1999 *The Laplace Transform: Theory and Applications*. Springer.

SHEIKHA, H., POOLADI-DARVISH, M. & MEHROTRA, A. K. 2005 Development of graphical methods for estimating the diffusivity coefficient of gases in bitumen from pressure-decay data. *Energy Fuels* **19**, 2041–2049.

SHI, Z., WEN, B., HESSE, M. A., TSOTSIS, T. T. & JESSEN, K. 2018 Measurement and modeling of CO_2 mass transfer in brine at reservoir conditions. *Adv. Water Resour.* **113**, 100–111.

SLIM, A. C. 2014 Solutal-convection regimes in a two-dimensional porous medium. *J. Fluid Mech.* **741**, 461–491.

SLIM, A. C., BANDI, M. M., MILLER, J. C. & MAHADEVAN, L. 2013 Dissolution-driven convection in a Hele-Shaw cell. *Phys. Fluids* **25**, 024101.

SLIM, A. C. & RAMAKRISHNAN, T. S. 2010 Onset and cessation of time-dependent, dissolution-driven convection in porous media. *Phys. Fluids* **22**, 124103.

SZULCZEWSKI, M. L., HESSE, M. A. & JUANES, R. 2013 Carbon dioxide dissolution in structural and stratigraphic traps. *J. Fluid Mech.* **736**, 287–315.

TILTON, N. & RIAZ, A. 2014 Nonlinear stability of gravitationally unstable, transient, diffusive boundary layers in porous media. *J. Fluid Mech.* **745**, 251–278.

TSE, F. C. & SANDALL, O. C. 1979 Diffusion coefficients for oxygen and carbon dioxide in water at 25 °C by unsteady state desorption from a quiescent liquid. *Chem. Engng Commun.* **3**, 147–153.

UNWIN, H. J. T., WELLS, G. N. & WOODS, A. W. 2016 CO_2 dissolution in a background hydrological flow. *J. Fluid Mech.* **789**, 768–784.

WANG, L. S., LANG, Z. X. & GUO, T. M. 1996 Measurement and correlation of the diffusion coefficients of carbon dioxide in liquid hydrocarbons under elevated pressures. *Fluid Phase Equilib.* **117**, 364–372.

WEIR, G. J., WHITE, S. P. & KISSLING, W. M. 1995 Reservoir storage and containment of greenhouse gases. *Energy Convers. Manage.* **36**, 531–534.

WEN, B. & CHINI, G. P. 2018 Inclined porous medium convection at large Rayleigh number. *J. Fluid Mech.* **837**, 670–702.

https://doi.org/10.1017/jfm.2018.622 Published online by Cambridge University Press

WEN, B., CHINI, G. P., DIANATI, N. & DOERING, C. R. 2013 Computational approaches to aspect-ratio-dependent upper bounds and heat flux in porous medium convection. *Phys. Lett.* A **377**, 2931–2938.

WEN, B., CORSON, L. T. & CHINI, G. P. 2015 Structure and stability of steady porous medium convection at large Rayleigh number. *J. Fluid Mech.* **772**, 197–224.

WEN, B., DIANATI, N., LUNASIN, E., CHINI, G. P. & DOERING, C. R. 2012 New upper bounds and reduced dynamical modeling for Rayleigh–Bénard convection in a fluid saturated porous layer. *Commun. Nonlinear Sci. Numer. Simul.* **17**, 2191–2199.

WILKES, K. E. 1995 Onset of natural convection in a horizontal porous medium with mixed thermal boundary conditions. *Trans. ASME J. Heat Transfer* **117**, 543–547.

XU, X., CHEN, S. & ZHANG, D. 2006 Convective stability analysis of the long-term storage of carbon dioxide in deep saline aquifers. *Adv. Water Resour.* **29**, 397–407.

ZECCA, M., HONARI, A., VOGT, S. J., BIJELJIC, B., MAY, E. F. & JOHNS, M. L. 2016 Measurements of rock core dispersivity and tortuosity for multi-phase systems. In *International Symposium of the Society of Core Analysts, Snowmass, Colorado, USA*, Society of Core Analysts.

ZHANG, L, HESSE, M. A. & WANG, M. 2017 Transient solute transport with sorption in Poiseuille flow. *J. Fluid Mech.* **828**, 733–752.

ZHANG, Y. P., HYNDMAN, C. L. & MAINI, B. B. 2000 Measurement of gas diffusivity in heavy oils. *J. Petrol. Sci. Engng* **25**, 37–47.

https://doi.org/10.1017/jfm.2018.622 Published online by Cambridge University Press